INL/EXT-15-36761 Rev. 0

September 2015

Multiscale Multiphysics Developments for Accident Tolerant Fuel Concepts

K. A. Gamble
J. D. Hales
J. Yu
Y. Zhang
X. Bai
D. Andersson
A. Patra
W. Wen
C. Tomé
M. Baskes
E. Martinez
C. R. Stanek
Y. Miao
B. Ye
G. L. Hofman
A. M. Yacout
W. Liu

INL/EXT-15-36761 Rev. 0

Multiscale Multiphysics Developments for Accident Tolerant Fuel Concepts

K. A. Gamble[1]
J. D. Hales[1]
J. Yu[1]
Y. Zhang[1]
X. Bai[1]
D. Andersson[2]
A. Patra[2]
W. Wen[2]
C. Tomé[2]
M. Baskes[2]
E. Martinez[2]
C. R. Stanek[2]
Y. Miao[3]
B. Ye[3]
G. L. Hofman[3]
A. M. Yacout[3]
W. Liu[4]

September 2015

[1]Idaho National Laboratory
[2]Los Alamos National Laboratory
[3]Argonne National Laboratory
[4]ANATECH Corp.

Fuel Modeling and Simulation Department
Idaho Falls, Idaho 83415

Prepared for the
U.S. Department of Energy
Office of Nuclear Energy
Under U.S. Department of Energy-Idaho Operations Office
Contract DE-AC07-99ID13727

Abstract

U_3Si_2 and iron-chromium-aluminum (Fe-Cr-Al) alloys are two of many proposed accident tolerant fuel concepts for the fuel and cladding respectively. The behavior of these materials under normal operating and accident reactor conditions is not well known. As part of the Department of Energy's Nuclear Energy Advanced Modeling and Simulation program, an Accident Tolerant Fuel High Impact Problem effort has been conducted to investigate U_3Si_2 and FeCrAl behavior under reactor conditions. This report presents the multiscale and multiphysics effort completed in fiscal year 2015. The report is split into four major categories: Density Functional Theory Developments, Molecular Dynamics Developments, Mesoscale Developments, and Engineering Scale Developments. The work shown here is a compilation of a collaborative effort between Idaho National Laboratory, Los Alamos National Laboratory, Argonne National Laboratory, and ANATECH Corp.

Contents

1 Introduction

In March 2011, a magnitude 9.0 earthquake struck off the coast of Japan. The earthquake and the associated tsunami resulted in tens of thousands of deaths, hundreds of thousands of damaged buildings, and a cost estimated to be in the hundreds of millions of dollars.

One consequence of the tsunami was the flooding of backup power generators at the Fukushima Daiichi Nuclear Power Station. The loss of power to coolant systems led to high temperatures, oxidation of Zr-based alloys, hydrogen production, melted fuel, and hydrogen explosions. As a result, a massive cleanup effort is underway at Fukushima Daiichi. The economic impacts, both those directly related to the cleanup and those affecting the nuclear energy sector generally, are significant.

Following the disaster, efforts to develop nuclear fuels with enhanced accident tolerance were begun by many nations, corporations, and research institutes. In the United States, the Department of Energy's Office of Nuclear Energy accelerated research on this topic as part of its Fuel Cycle Research and Development (FCRD) Advanced Fuels Campaign (AFC). One product of this work is Light Water Reactor Accident Tolerant Fuel Performance Metrics [1], a report by AFC that outlines a set of metrics that can be used to guide selection of promising accident tolerant fuel (ATF) concepts. Furthermore, [1] specifies that a down-selection is to occur in the 2016-2017 timeframe, at which time the program will move from a proof-of-concept stage to a proof-of-principle stage and continue research and development on a small set of concepts.

Given the aggressive development schedule, it is impossible to perform a comprehensive set of experiments to provide material characterization data. Therefore, the AFC plans to utilize computational analysis tools in an effort to understand the proposed materials.

The Nuclear Energy Advanced Modeling and Simulation (NEAMS) program in DOE has for some time been developing computational analysis tools. These include BISON [2–4] and Marmot [5], analysis tools tailored to nuclear fuel at the engineering scale and grain scale, respectively. Recently, NEAMS has introduced what it calls High Impact Problems (HIPs) into its program plan. These HIPs are intended to make a significant advance in a particular area of nuclear power research in a short period of time (3 years or less). NEAMS has chosen an ATF project, which emphasizes utilizing BISON and Marmot to model proposed materials, as its first HIP. This report focuses on the multiscale and multiphysics developments of ATF fuel concepts through the ATF HIP. Participating national laboratories include Idaho National Laboratory (INL), Los Alamos National Laboratory (LANL), Argonne National Laboratory (ANL), and ANATECH Corp.

2 Density Functional Theory Developments

2.1 Density functional theory calculations of defect and fission gas properties in U-Si fuel

We have investigated point defect and fission gas properties in U_3Si_2, which is one of the main ATF fuel candidates, using density functional theory (DFT) calculations. Based on a few assumption regarding entropy contributions, defect and fission diffusivities are also predicted.

The DFT calculations were carried out with the VASP code [6–8] using the projector augmented-wave (PAW) method and Perdew-Burke-Ernzerhof (PBE) [9] potentials for the exchange-correlation potentials. This methodology has been shown to work well for the U and Si end-member systems. However, initial calculations showed that the U_3Si_2 crystal structure is not stable within the PBE method. This is not obvious from calculations on the unit cell, but phonon calculations give negative frequencies and calculations on the 222 supercell relaxes to a distorted structure with much lower energy (0.10 eV/atom). The original and new relaxed structures are shown in Figure 2.1. There is, however, no experimental support for breaking the symmetry of the U_3Si_2 crystal structure (space group P4/mbm), which suggests that the DFT calculations fail to capture some important physics. The most obvious suspect is the U 5f electrons, which are known to exhibit strong correlation effects. There are several ways to describe the strongly correlated properties of the U 5f electrons, such as the Hubbard U method. Here we have applied the Hubbard U (PBE+U) method [10] due to its simplicity and computational efficiency. The value of the U parameter is not known *a priori*. We tested several different U values ranging from 0 to 3 eV. For values of 1.5 eV or higher the distorted structure is no longer stable and relaxes back to the experimental structure with the space group P4/mbm. The stability of the U_3Si_2 structure seems to be related to splitting or localizing the U 5f electrons for $U > 1.5$ eV. Defect properties were calculated in a $2\times2\times2$ supercell expansion of the U_3Si_2 unit cell using the PBE+U methodology.

In order to investigate fission gas diffusion and release, the probability of Xe (the most important fission gas) atoms occupying different lattice positions must be determined, which is equivalent to the fraction of Xe in that trap site. This involves two components, the formation energy of the trap site (e.g. formation energy of vacancies) and the incorporation energy (the energy associated with adding Xe to the trap site). The sum of these two components is labeled the solution energy. The trap site with the lowest solution energy is the preferred location for Xe in the lattice. The preferred trap site for Xe is U vacancies, but Si vacancies are only higher by a few tenths of an eV.

We have calculated the migration energies for U and Si interstitial and vacancies. There are a

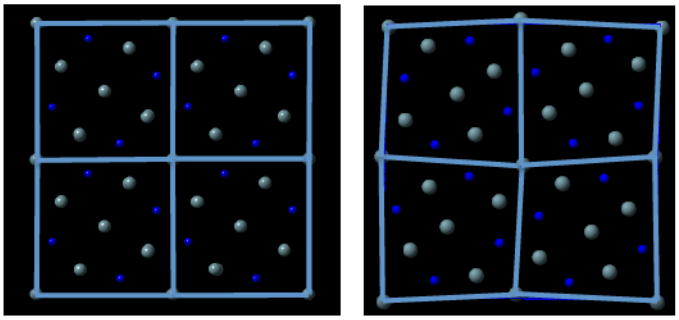

Figure 2.1: The relaxed structure of the $2\times2\times2$ U_3Si_2 supercell (left). The structure is visualized in the a-b plane with the c axis perpendicular to this plane. The crystal structure has two different U sites, labeled 1 and 2 in the text. The ideal $2\times2\times2$ U_3Si_2 supercell (right). The PBE method predicts the relaxed structure to have much lower energy than the ideal structure in Figure 2.1 (0.10 eV/atom).

couple of different vacancy mechanisms because of the symmetry of the U_3Si_2 crystal structure; in particular, diffusion may occur along the c axis or in the a-b plane. Our calculations show that migration along the c axis is much faster than in the in-plane a-b mechanisms. Diffusion of Xe involves migration of Xe from one lattice site to another, which is governed by the concentration of mobile clusters, i.e., the concentration of vacancies bound to the Xe trap site for vacancy mechanisms, and the migration barrier for the rate limiting diffusion step. We have investigated both interstitial and vacancy Xe diffusion mechanisms. For the vacancy mechanisms, the concentration of vacancies available at the trap site must be calculated. This is expressed by the vacancy formation energy and the binding energy of the vacancy to the Xe trap site. As for point defect migration, Xe migration along the c axis occurs much easier than within the a-b plane. The resulting diffusivities for point defects and Xe are plotted in Figure 2.2. The intrinsic and radiation-enhanced diffusion coefficients for UO_2 are also included for comparison. Both Xe atoms and vacancies diffuse much faster along the c axis than within the a-b plane. Diffusion of Xe along the c axis is faster than in UO_2, while in-plane Xe diffusion is slightly slower.

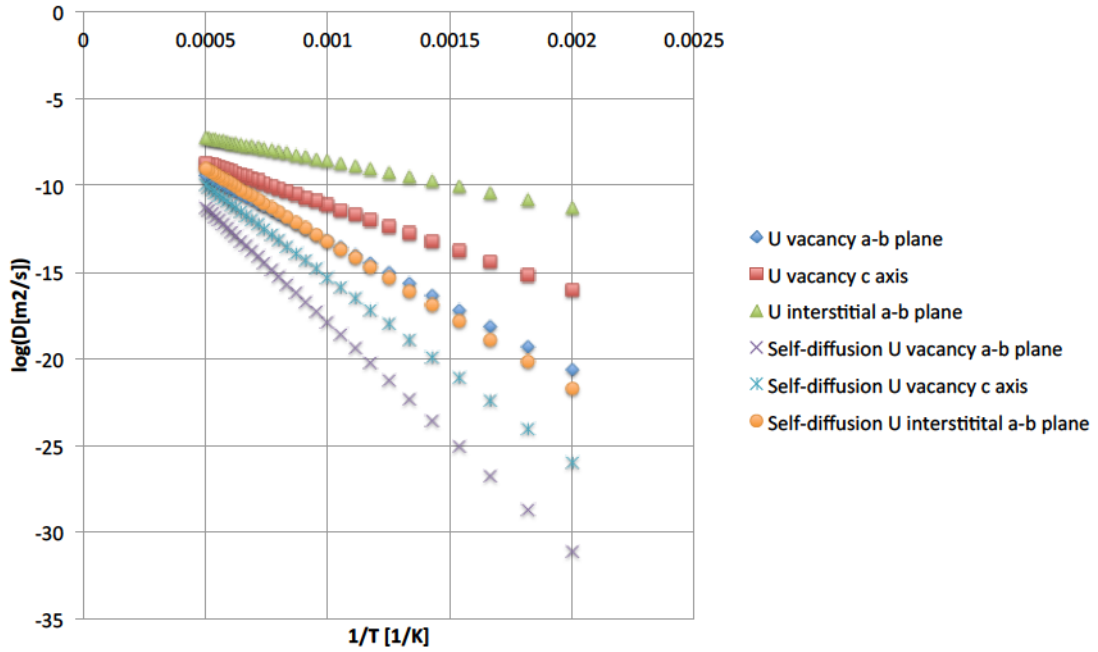

(a)

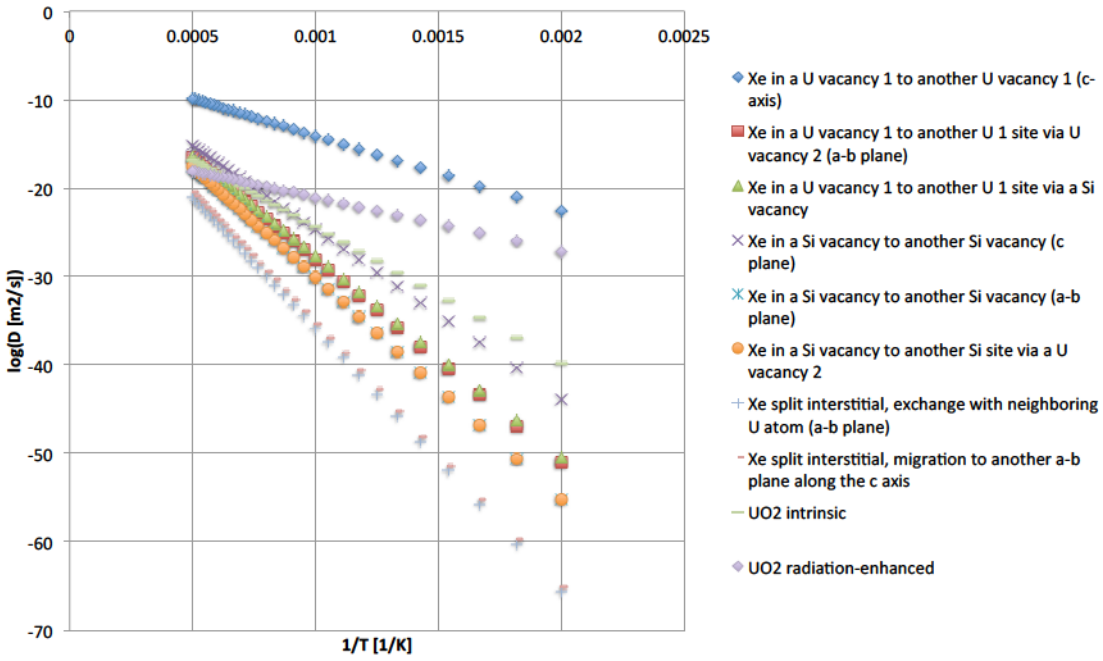

(b)

Figure 2.2: Uranium vacancy and uranium interstitial diffusivities as well as the corresponding self-diffusion coefficients (a). The latter include the vacancy and interstitial formation energies. Calculated intrinsic Xe diffusivities for different mechanisms in U_3Si_2 (b). The intrinsic and radiation-enhanced diffusion coefficients for UO_2 are also included for comparison.

3 Molecular Dynamics Developments

3.1 Assessment of semi-empirical potentials for the U-Si system

In order to perform meaningful engineering scale nuclear fuel performance simulations, the material properties of the fuel, including the response to irradiation environments, must be known. Unfortunately, the data available for U-Si fuels are rather limited, in particular for the temperature range where LWRs would operate. The ATF HIP is using multi-scale modeling and simulations to address this knowledge gap. Even though Density Functional Theory (DFT) calculations can provide useful answers to a subset of problems, they are computationally too costly for many others, including properties governing microstructure evolution and irradiation effects. For the latter, semi-empirical potentials are typically used. Unfortunately, there is currently no potential for the U-Si system. We present initial results from the development of a U-Si semi-empirical potential based on the Modified Embedded Atom Method (MEAM). The potential should reproduce relevant parts of the U-Si phase diagram (see Figure 3.1) as well as defect properties important in irradiation environments. This work also serves as an assessment of the general challenges associated with the U-Si system, which will be valuable for the efforts to develop a U-Si Tersoff potential undertaken by Idaho National Laboratory. Going forward the main potential development activity will reside at INL and the work presented here is meant to provide input data and guidelines for that activity. The main focus of our work is on the U_3Si_2 and U_3Si_5 compounds, because they are the main nuclear fuel candidates.

In order to develop a potential for the binary U-Si system we must start from the unary U and Si systems. In this work, we have used a U potential from recent work with INL/GA Tech (M. Baskes) and for Si we used a potential from the literature [12]. The U-Si parameters needed to describe the binary system can either be fitted to available experimental data or to data derived from DFT calculations. Here we used a combination of the two to fit the MEAM cross potential. The MEAM parameters that were fitted or adjusted here are highlighted in red in Table 3.2 and include the relative electron densities, the heat of formation for the L_{12} reference structure, the distance between atoms in the reference structure and the α parameter for the pair potential between U and Si, which is related to the bulk modulus of the L_{12} reference structure, a cubic repulsive term in the U-Si Rose pair potential as well as the MEAM screening parameters capturing how a third atom screens the interaction between two other atoms. The latter introduces many-body interactions necessary for systems exhibiting complicated crystal structures such as U, Si and several compounds in the U-Si system. These parameters are summarized in Figure 3.2, utilizing the standard notation for MEAM potentials.

Many different properties have been calculated using the MEAM potential and used in the fitting. This includes formation energies, volumes elastic constants, defect formation energies and

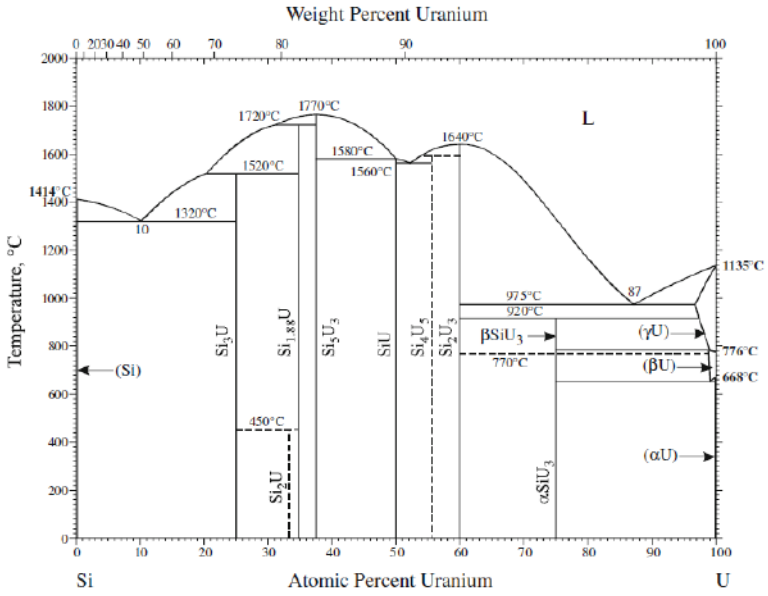

Figure 3.1: Experimental U-Si phase diagram [11].

```
$meacard ntypes=2, legend=0.6 enames(1)='UM','Sis',
kodes(1)='library','library',
repuls(1,1)=0.105,attrac(1,1)=0.105 cmin(2,2,2)=2.0
cmin(1,1,1)=1.0 cmax(1,1,1)=1.9
xncut=2.0,xmcut=6.0,rcut=5.0,nn=.t.,ialloy=1
rozros=1.00,1.7
alphas(1,2)=4.4,deltas(1,2)=-0.5,all(1,2)='L12' res(1,2)=3.046
repuls(1,2)=0.20, cmin(2,1,2)=0.2,cmax(2,1,2)=1.2
cmin(1,2,1)=2.0,cmax(1,2,1)=2.8
cmin(1,1,2)=2.0,cmax(1,1,2)=2.8
cmin(1,2,2)=2.0,cmax(1,2,2)=2.8 &end

Red determined from fit to DFT-U and experiments in this
work.
```

Figure 3.2: MEAM cross terms for the U-Si potential derived in this work. The red parameters were adjusted or fitted in this work. All others were left at default values.

finite temperature dynamics. As reference we use results from both DFT calculations and experiments. For example, the stability of a range of U-Si phases was calculated with reference to α uranium and silicon in the diamond structure. The DFT and MEAM data are shown in Figure 3.3 together with available experimental formation energies [13]. The DFT calculations agree well with the experimental formation energies across the full composition range. Even though the MEAM potential does a decent job for U_3Si_2 and U_3Si_5, several other phases are predicted to be too stable in relation to the DFT calculations and experiments. Also, there is an alternative U_3Si_2 structure that MEAM predicts to be more stable than the experimental structure; however, this is not confirmed by DFT. In summary, even though the formation energies are accurate for the U_3Si_2 and U_3Si_5 compounds the complex bonding in the U-Si system renders a complete description of the phase diagram very challenging.

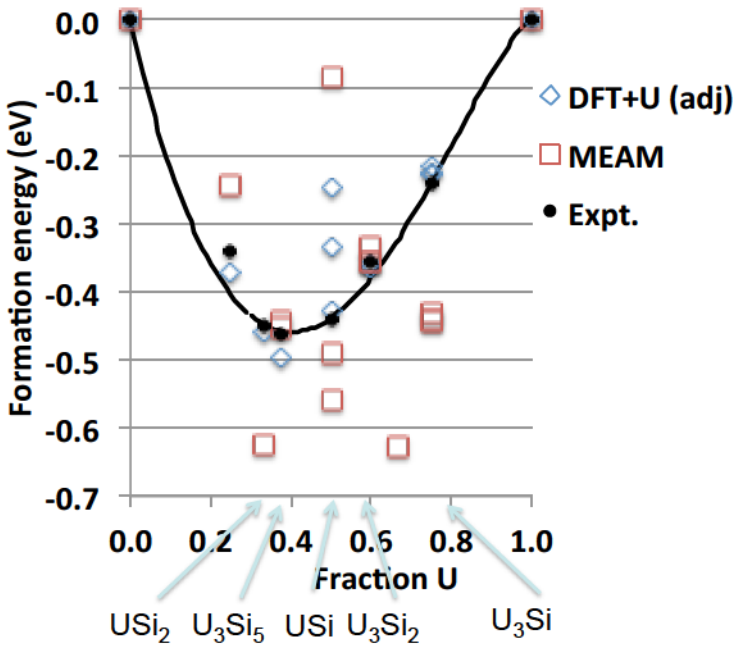

Figure 3.3: Formation energies for U-Si compounds (with respect to Si in the diamond structure and α uranium) as function of uranium fraction obtained from the MEAM potential, DFT calculations and experimental literature values [13]. The values are normalized per atom.

The MEAM potential was successful in capturing the stability and structure of the two main U_3Si_2 and U_3Si_5 fuel candidates. However, the complex bonding in this system gives rise to a complicated phase diagram and the potential fails to accurately predict the stability for some of the other U-Si phases. The MEAM potential also predicts competing stable phases at the U_3Si_2 composition that have not been confirmed by DFT calculations or experiments. This is going to cause problems in finite temperature molecular dynamics simulations. Additional work is required to resolve these issues. The volumes, elastic constants and defect properties predicted

by the MEAM potential also deviate from DFT calculations and experiments for several cases. All of these discrepancies are likely connected and we are currently focusing on improving the description of the volume of the USi_2 compound (AlB_2 structure), since that seems to be the root cause of many of the observed discrepancies. Despite the challenges that have been identified, our initial assessment of the possibility of developing a reliable U-Si potential has demonstrated some promising results and we are continuing to improve the MEAM potential. The results will also be provided as feedback to the development of a U-Si Tersoff potential at Idaho National Laboratory.

3.2 Development of MD potential for uranium silicide fuels

Low-enriched uranium-silicide dispersion fuel is used extensively worldwide in research and test reactors. U_3Si_2 is widely used mainly due to lower fission gas bubble growth and fuel swelling in U_3Si_2 than in U_3Si. The BISON group has already developed empirical models for thermal conductivity, specific heat, and swelling of U_3Si_2. To increase the predictive capabilities of these models, it is imperative to formulate in developing knowledge-based process models with a minimum of empirical parameters. For example, silicide compounds (U_3Si_2 and U_3Si) are known to become amorphous under irradiation. Such a transformation resulted in changes in fission gas mobility and the plastic flow rate [can be treated in Marmot either by crystal plasticity or continuum yield/stress/strain plasticity] of the fuel that were responsible for the large swelling increases. There was clear independent experimental evidence to support a crystalline to amorphous transformation in those compounds. However, it is still not well understand how the amorphous transformation will affect on the fuel behaviors. Thus an atomistic level understanding is warranted.

One of the most important variables in the performance of U_3Si_2 is the existence of the so-called secondary phases, such as U solid solution (α,β, γ), U_3Si (α,β), or U-Si. In order to develop knowledge-based model with a minimum of empirical parameters in BISON and Marmot, inputs from atomistic simulations are essential. DFT will provide most reliable information. However, due to the size and time limitation, kinetic information such as amorphization under irradiation directly from DFT is probably ruled out and the feasible way is from MD simulation. Unfortunately, so far no such MD potential is available for uranium-silicide to generate data. Thus we will develop uranium-silicide potential from *ab initio* data.

In order to investigate how uranium-silicide becomes amorphous under irradiation using MD simulation, it is crucial to have an appropriate MD potential formula capable of describing various crystallographic phases and amorphous states well. Comparing existing MD potentials for U and Si, the potential formalism we decide to adopt is the modified Tersoff potential [14], which so far is the best MD potential to study liquid or amorphous Si, besides various crystallographic phases. Since the parameter set for Si is available, only two additional parameter sets or interactions (U-U and Si-U) need to be fitted for U-Si potentials.

We will use POTFIT, a force matching potential fitting package, to fit the potential parameters.

This package has been built and installed at INL. Also it is instructive to consider the uncertainty quantification of the particular potential parameters. To this end, we tested how the sensitivity and range of potential parameters affect the fitting results and narrowed down the range for each parameter needing to be fitted.

POTFIT requires all input datasets such as lattice, energy and force directly from first-principles DFT calculations. However, it is difficult to obtain high fidelity force information from DFT due to the combination of a strong electron correlation, multiple minima and relativistic effects of 5f valence electrons of U.

In order to develop a rigorous, systematical and transferable potential, we also collected the dataset for the hypothetical structures of U, including dimer and tetramer at a variety of compressive and tensile strains. We note that under a thermalized or dynamical environment, the controlled environment of the atom utilized in the potential fitting process (static) will most probably be lost. In order to overcome this issue to describe the kinetic behavior with high fidelity, our datasets also include information about atoms displaced from the perfect crystal structures with respect to the crystal symmetry.

We collected the necessary datasets of energy, force and external stress for α, β , and γ phases of U at various conditions of hydrostatic strain (tensile/compressive). Figure 3.4 shows the potential energy-volume (E-V) curve for (α,β, γ)-U. We found that at 0K, α-U is most stable, β-U is about 0.1 eV/atom higher, and γ-U is about 0.27 eV/atom higher than α-U. Meanwhile, we also found that for γ-U under tensile strain, a magnetic structure is more energy favorable than that of the non-magnetic structure. Experimentally validating this may be valuable.

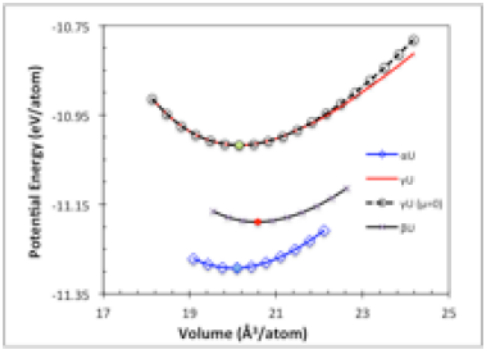

Figure 3.4: E-V for α, β and γ-U

Free energy of these phases as a function temperature is also calculated. First principles calculations based on the quasi-harmonic approximation are adopted here. We used the VASP software for the first principles calculations. Energy derivatives such as force were extracted from VASP results, and such information is required to calculate C_p, for example. Both Rose-Vinet and third-order Birch-Murnaghan equation of state (EOS) were used fit the derived thermal properties of U phases. α-U is stable up to 935 K. It is orthorhombic with space group Cmcm (#63).

In α-U each primitive cell (PC) contains 2 atoms and two PCs form a unit cell. According to the crystal symmetry, phonon calculations will need two types of displacement per unit cell besides the ideal structure. A 4x2x2 unit cell is used for the calculations of thermal properties for α-U and there are 57 different structures calculated. The result of thermal properties for α-U phase is plotted as shown in Figure 3.5. The structure of α-U phase is very complex which may be visualized as corrugated rectangular layers stacked in the [010] direction. For the α-U phase, as temperature increases, bulk modulus will decrease, reach the minimum at ∼100K, then increase. The specific heat C_p will reach a near plateau region as the temperature is above ∼250 K. The volume of α-U will be maximum at ∼500K, then collapse.

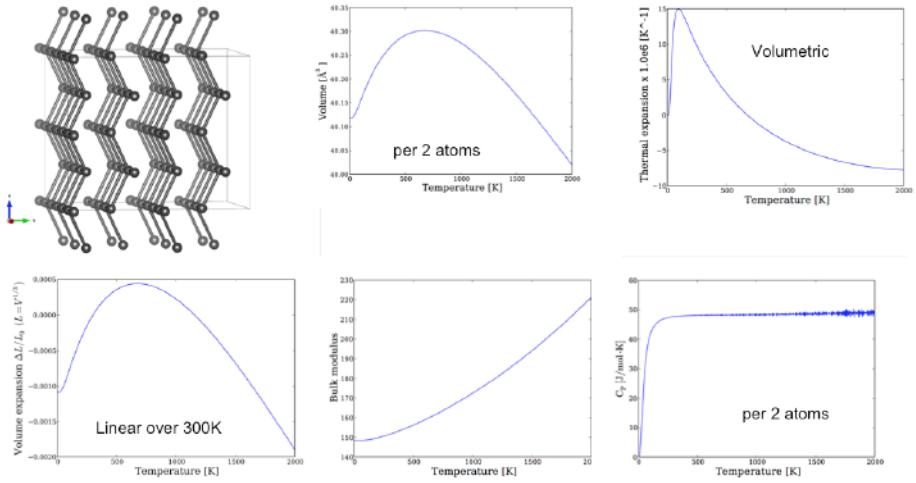

Figure 3.5: α-U thermal properties

We also investigated the thermal properties of the β-U phase. β phase is stable from 935 to 1045 K for pressures up to 3 GPa, with centro-symmetric space group P42/mnm (#136). It has a very complicated tetragonal structure with 30 atoms per PC. In order to obtain the thermal properties of β-U phase, 15 types of displacement are needed for each structure containing two PCs with a total number of 160 different structures calculated here. The structure may be imaged as the packing of layers of irregular five-member rings in the c-direction as shown in Figure 3.6. Figure 3.6 also shows the result of thermal properties for β-U phase.

- We found that for β-U phase as temperature increases, bulk modulus will decrease, from ∼130 GPa to 240 GPa at 2000 K.
- The specific heat C_p will increase from 0 J/mol/K at 0 K, and reach a near plateau region at 700 J/mol/K as the temperature is above ∼250 K. Note for β-U phase, there are 30 atoms per primitive cell.
- The thermal expansion of β-U will increase from 0 /K at 0 K, reach a maximum (∼1.7×10-6 /K) at ∼100K, then reduce, and become negative above ∼1800 K.

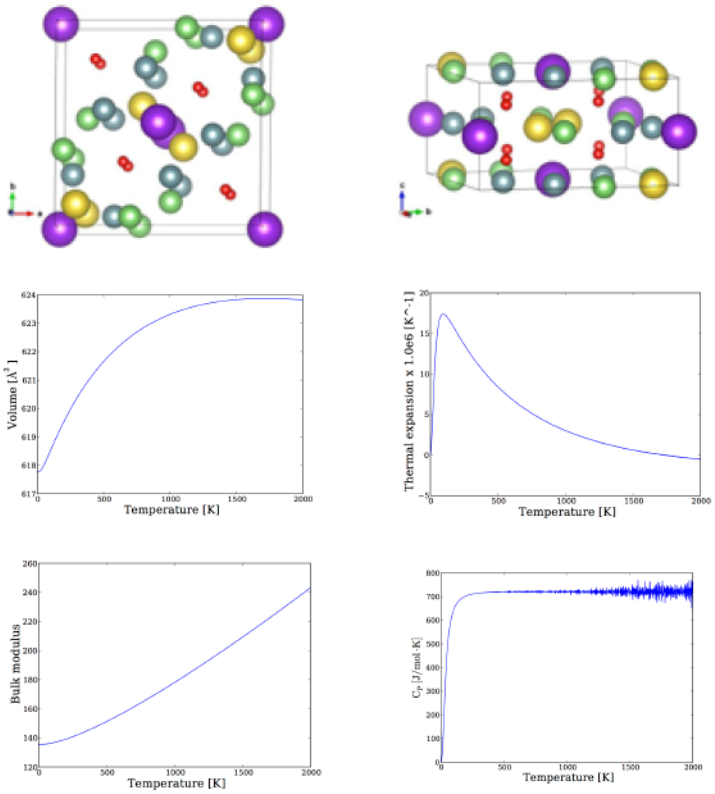

Figure 3.6: β-U thermal properties

The result of γ-U thermal properties is shown in Figure 3.7. We found that for γ-U phase as temperature increases, bulk modulus will decrease, reach the minimum at ∼90K, then increase. Meanwhile, the volume of γ-U will be maximum at ∼110K, then collapse. It is apparent that γ-U is unstable at low temperature. Furthermore investigation of high temperature thermal properties of γ-U is underway.

We fitted and evaluated the 16 potential parameters based on the modified Tersoff potential for U. Fitting from a database of ∼259 configurations (57 α-U, 160 β-U, 38 γ-U, and 4 U tetramers), ∼50000 forces and ∼1560 stresses, we have obtained many parameter sets by varying the weigh factor of each data point and then evaluating the potential parameters. Figure 3.8 shows the result predicted by one of our fitting parameter sets. As one can see, so far the prediction of potential energies for α, β, γ-U align with DFT results well. Meanwhile the issues such as the lowest energy phase being γ-U phase rather than α-U phase is lifted by the improved parameter set, and all fitting phases of U are correct. Furthermore, as one can see, β-U phase is described very well by our potential. Regarding the transferability, the U potential developed in this project already surpasses all existing U potentials.

To pursue the maximum transferability of the fitting potential, we also prepared test and valida-

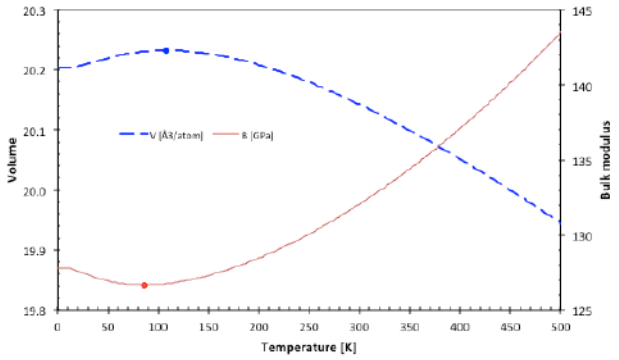

Figure 3.7: γ-U thermal properties

tion datasets by DFT calculations to collect the energy vs. volume for other unfitted structures. The testing structures of U are the hypothetical phases of U diamond, simple cubic (SC) and face center cubic (FCC). However, it is extremely difficult to maximize the transferability and accuracy of all phases, and some compromise may be necessary. More detail will be presented in the near future.

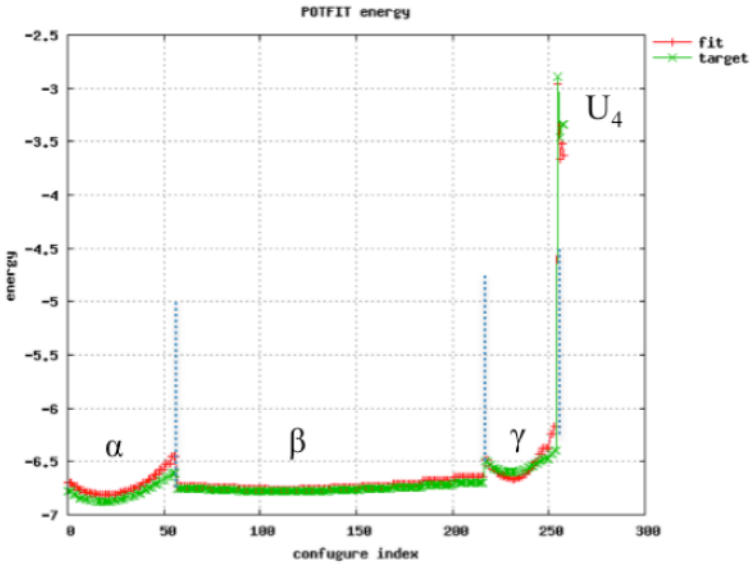

Figure 3.8: Potential energy surface of α, β, γ-U and U4 tetramer at various strains predicted by our fitting parameter set and compared with DFT results.

4 Mesoscale Developments

4.1 Modeling the irradiation hardening behavior of FeCrAl alloys using crystal plasticity simulations

We have implemented a defect density-based constitutive crystal plasticity model [15, 16] in the Visco Plastic Self Consistent (VPSC) framework [17] to simulate the mechanical response of FeCrAl alloys post-irradiation. Irradiation induced defects including $< 111 >$ and $< 100 >$ dislocation loops, and α' precipitates are used as state variables in this framework and constitutive models implemented to simulate the observed deformation behavior. The model parameters have been calibrated to tensile loading experiments performed at ORNL [18–20]. The model was first calibrated to the true stress-strain response of a virgin (no irradiation) Fe-15Cr-4Al alloy. Figure 4.1(a) shows the comparison of model predictions with the experimental stress-strain data at room temperature. A reasonable correlation to experiments was obtained up to true strains of 0.4. Model parameters related to the irradiation damage were then calibrated using defect densities for the Fe-15Cr-3.9Al alloy given in [19, 20]. The model was then used to predict the irradiation hardening behavior for alloys with varying compositions. Figure 4.1(b) shows the comparison of model predictions of the initial yield stress with experiments for alloys irradiated to 1.6 dpa damage. The model is able to reproduce the observed increase in yield stress due to irradiation hardening with reasonable confidence. Moreover, the subsequent hardening behavior (not shown here) is consistent with experiments, where the stress-strain response flattens out following initial yield.

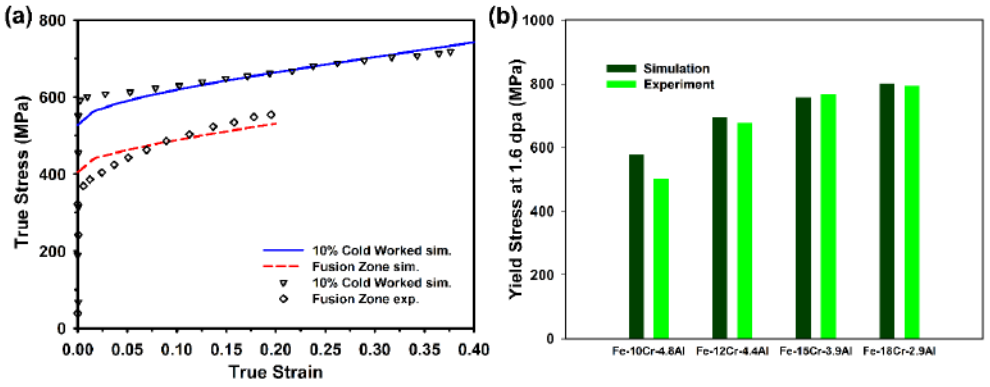

Figure 4.1: (a): Model predictions of the stress-strain response of cold worked and fusion zone specimens of Fe-15Cr-4Al laser weld alloys compared with experiments [18], (b): Comparison of the predicted yield stress with experiments [19, 20] for various Fe-CrAl alloys irradiated to 1.6 dpa damage.

We are presently working on implementing these models in the BISON finite element framework. This model will allow us to simulate reactor conditions similar to Loss of Coolant Accident (LOCA). Physically based irradiation creep and thermal creep models will also be incorporated in this framework in the next phase of the project.

4.2 Rate Theory Model of the Swelling Behavior of Canadian U_3Si Fuel

Accurate prediction of the fission gas bubble evolution during irradiation and its interrelation with the macroscopic radiation-induced swelling behavior of U_3Si_2 fuel is crucial for the development and design of the fuel elements. DART/GRASS-SST [21, 22], a rate theory code which has been successfully applied to interpret the experimental observations of U_3Si_2 and U_3Si fuel swelling in both plate and rod fuel element geometries, is employed to predict the swelling behavior of U_3Si_2 in this project. As the first step, the reliability and accuracy of the codes in handling silicide fuel materials shall be examined and validated based on existing data. The information obtained from the rate-theory modeling is also beneficial for understanding the underlying mechanisms of silicide fuel swelling by using atomic-scale material simulation tools.

Due to the lack of experimental swelling data of U_3Si_2, U_3Si was selected instead in this study as the first attempt to use the rate theory gas behavior model in DART/GRASS-SST for uranium silicide fuel swelling simulation at high operating temperatures (500°C). Canadians measured the swelling behaviors of U_3Si in 1960s [23]. Those data were used for the comparison with the calculation results.

U_3Si rods cladded by Zircaloy-2 with central voids were irradiated in the X-5 loop of the Chalk River NRX Reactor up to 6000 MWd/tU. The swelling was monitored throughout the test (see scattered points in Figure 4.2). The fuel swelling can be divided into two stages. In the first stage, the increased volume mainly fills the central void and the gap rather than interact with the cladding. In the second stage, however, the fuel swelling is constrained by the cladding. In this study, the first stage was used to tune the material parameters that determine the gas swelling rate without constraints. Then a simple fuel-cladding interaction model was established to replicate the swelling behavior in the second stage and to examine the feasibility of coupling DART/GRASS-SST and BISON.

In this study, the mechanistic fission-gas release and swelling model GRASS-SST [24] was employed for U_3Si pellet swelling simulation . GRASS-SST is the basis of the dispersion fuel performance code DART [25, 26], whose capability in simulating fission gas behavior in fuels has been validated extensively [24–27]. The primary reason for using GRASS-SST instead of DART in this project is that DART considers the complex particle-matrix interaction in a dispersion fuel system, which is irrelevant for monolithic fuels.

GRASS-SST models the effects of fission-product generation, atomic migration, bubble nucleation and re-solution, bubble migration and coalescence, interlinked porosity, and fission-gas

interaction with structural defects [24]. GRASS-SST calculates the fission-gas-bubble-size distribution for bubbles in the lattice, on grain boundaries, on dislocations, and along the grain edges by solving a set of coupled nonlinear differential equations [28]. Besides the environment parameters such as temperatures, burnup, and geometry, those equations are also controlled by several key material properties. Due to the scarce available data on U_3Si materials properties, some of the values of the material parameters were taken from UO_2 fuel [27], and others have to be tuned to fit to the measurements, such as gas atom diffusivity (D_g), bubble nucleation factor on grain boundary (f_n), resolution rate (b_0) and fuel surface energy (γ). Sensitivity examinations were performed for all the tuned values. Results show that D_g [29], and f_n have strongest effects on the swelling behavior. It is critical to check the physics models and verify the values of materials properties used in the current rate-theory code by using the lower scale computation methods or/and single effects experiments.

For simulating the first stage in fuel swelling (before gap closure), no modifications on the physics models in the code were made; some materials properties were adjusted. The resultant fuel swelling reasonably agrees with the measured volume increases as shown in Figure 4.2. For simulating the second stage in fuel swelling (after gap closure), a simple mechanical model is implemented to emulate the cladding effect. Multiple deformation mechanisms, including elasticity, plasticity and thermal/irradiation creep of Zircaloy-2 were quantitatively analyzed based the experimental data [30]. Irradiation creep [31] was found to dominate the second stage. The fuel pressure in the second stage was tuned within the range that can be reasonably provided by the Zircaloy-2 cladding under irradiation creep [32]. The results are consistent with the experimental data. Swelling behavior in both stages now can be replicated by GRASS-SST, as shown in Figure 4.2.

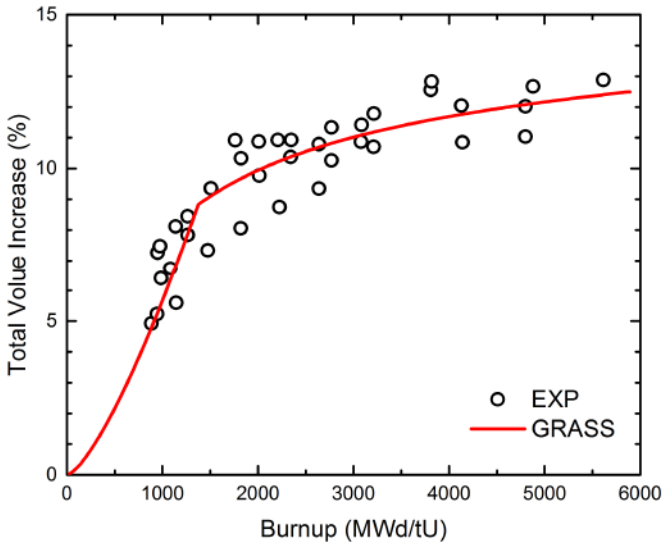

Figure 4.2: Rate theory predicted swelling rate compared with the experimental measurement

However, realistic fuel-cladding interaction is much more complex. Adopting more complex models with advanced algorithm such as FEM will further improve the reliability and accuracy of current rate theory calculation. Therefore, coupling GRASS with BISON will expand the capability of this code. As we have already succeeded in coupling Fast-GRASS, a light version of GRASS which ignores the size distribution of gas bubbles, with BISON, we have sufficient experience in handling similar activities.

In this study, we tuned the parameters in GRASS-SST to replicate the experimentally measured swelling data in U_3Si fuel with Zircaloy-2 cladding at LWR operating conditions. A parameter sensitivity test was performed for a series of material parameters to show how these key material properties influence the swelling behavior without taking into account the cladding restraining effects. The code successfully replicates the radiation-induced swelling behaviors of U_3Si. Also, the simulation shows it is important to obtain some reliable parameters from either lower-scale simulations or experiments to improve the reliability of the rate theory code and provide initial improved parameters estimates to Marmot code. A simplified model was also established to predict the swelling behavior considering the interactions between the Zircaloy-2 cladding and U_3Si fuel. The results match the measured data, demonstrating the potential of GRASS-SST in predicting fuel swelling behavior influenced by cladding with the help of external model. This also emphasizes the importance of the coupling between GRASS and BISON to establish a package with comprehensive functionality to predict the fuel behavior at higher burnups.

4.3 Evaluation of microstructure impact on the thermal conductivity of U_3Si_2 using Marmot

INL has recently developed various capabilities to measure the thermal conductivities of a wide range of fuels, including the thermal conductivity microscope (TCM) for measurements at the microscale ($\sim\mu$m) and standard laser flash for measurements at the scale of fuel pins. These two methods have been applied to several types of fuels including U_3Si_2 fuel, which is a promising candidate for accident tolerant fuels. The measured thermal conductivity for a U_3Si_2 fuel sample recently fabricated at INL by these two methods differed from each other slightly. This difference suggests the impact of microstructure on the measurement, since these two methods work at difference spatial scales. The TCM method measures the conductivity and diffusivity locally for the U_3Si_2 matrix, while the laser flash method measures the overall conductivity of the fuel, which consists of more complex microstructure. Here, modeling using the Marmot code was conducted to reconcile the results from these two methods by considering the impact of microstructure. The Marmot code is a powerful tool for calculating the effective thermophysical properties of material systems with complex microstructures.

The fabricated U_3Si_2 fuel is not pure. Various phases other than the U_3Si_2 matrix have been identified, as indicated by contrast in the SEM image. Analysis of the chemical elements indicates that in addition to the U_3Si_2 matrix, two other phases may also exist: USi and an oxide phase, either U_3O_8 or hyper-stoichiometric UO_2 to be cleared in the future by further characterization (4.3a). Here our modeling focuses on the impact of the oxide phase which has a much

lower conductivity than those of the U-Si phases. In the modeling, we distinguished the oxide phase from the rest by reconstructing the SEM image using the image-processing tool in MOOSE (4.3b). Mesh adaptivity has been enabled at the interface. Based on the reconstructed mesh, the Marmot code was used to calculate the effective thermal conductivity at room temperature. For the U_3Si_2 matrix, we took the value of 8.9 W/m-K from the TCM measurement. For the oxide phase, two calculations were done by taking the phase to be either U_3O_8 or hyperstoichiometric UO_2. A value of 2.2 W/m-K from literature [33] was used for U_3O_8, and that of 4.3 W/m-K [34] was used for UO_2. The results showed that the discrepancy between the results from TCM and laser flash measurements can be explained (4.3c) by considering the impact of the microstructure of the sample, i.e., the appearance of the oxide phase. (This may also explain why the INL measurements are lower than the LANL results which were obtained with purer U_3Si_2 samples [35]. We believe that better comparison can be achieved in the future with further consideration of the microstructural details.

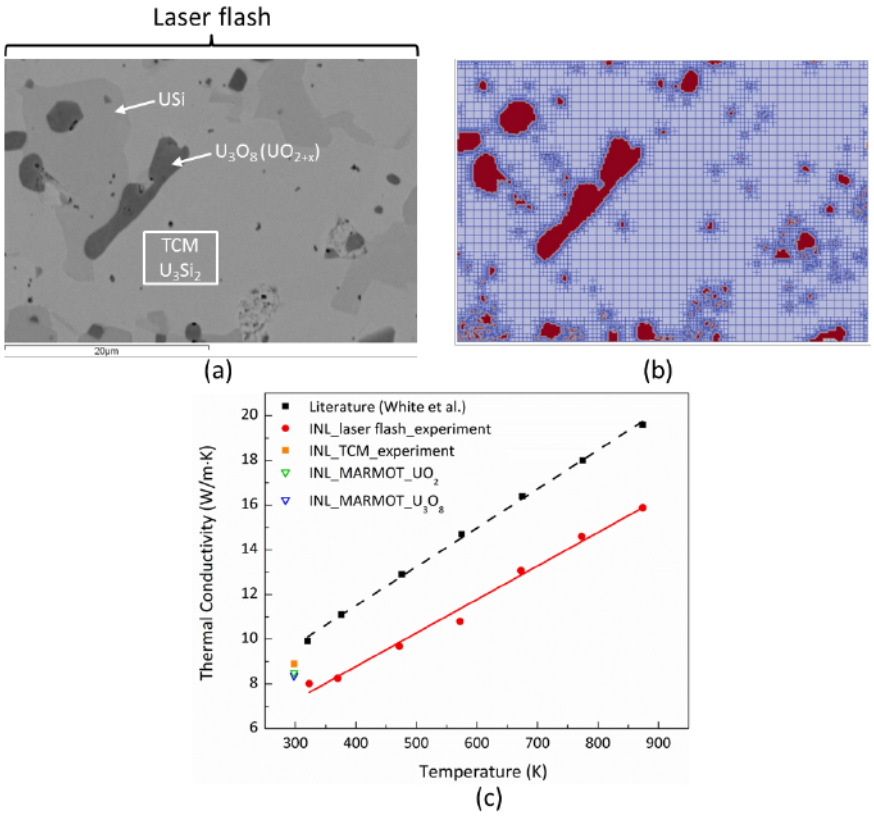

Figure 4.3: (a) SEM image of a U_3Si_2 sample, (b) reconstructed microstructure and mesh in MOOSE for Marmot calculations, and (c) thermal conductivity of U_3Si_2 as a function of temperature. The solids symbols are experimental measurements from literature and INL. The TCM result is shown as the solid square. The Marmot results based on the reconstructed mesh are represented by the open triangles.

5 Engineering Scale Developments

Material behavior and properties of interest at the engineering scale include: thermal conductivity, specific heat capacity, Young's modulus, Poisson's ratio, thermal expansion, fission gas release, fuel and cladding swelling, and thermal and irradiation creep. It is important to note that many of the engineering scale parameters of interest are influenced by phenomena occurring at the lower length scales. The density functional theory, molecular dynamics, and mesoscale developments in FY 2015 as part of the ATF HIP were presented in previous chapters, demonstrating that the capabilities are still under development. Therefore, at this stage the engineering scale studies were completely decoupled from the lower length scale activities until further developments are completed. The ATF fuel concepts studied include uranium silicide compounds and iron-chromium-aluminum (Fe-Cr-Al) alloys. Since experimental data is limited for these materials, the engineering scale research focused on sensitivity analyses and bounding studies on critical material parameters using the BISON fuel performance code while utilizing available data and expert judgment.

5.1 Uranium Silicide

Uranium silicides are leading candidates for the fuel in accident tolerant fuel rods. U_3Si_2 has a number of advantageous properties compared to UO_2. In particular its higher density and thermal conductivity enable the fuel to operate a much lower temperatures and thermal gradients. This results in lower thermal stresses within the fuel, which should mitigate pellet cracking [36]. Less cracking and lower temperatures should result in much lower fission gas release into the plenum regions than with UO_2 fuel. One disadvantage of uranium silicide is that almost all of the experimental data that is available is for experimental dispersion fuels, not monolithic fuel as would be present in an LWR. This raises the question of whether the data is appropriate for monolithic fuel and can be used in modeling. Furthermore, there is limited data on fission gas mechanisms, creep, and densification behavior in uranium silicides. This section presents the material models included in BISON for uranium silicide and highlights the sensitivity analyses and bounding studies completed.

5.1.1 Material Models

BISON is built upon the MOOSE computational framework which provides a relatively simplistic methodology for implementing new material and behavior models into the code. The material models available in BISON for U_3Si_2 include temperature dependent thermal conductivity and specific heat capacity and burnup dependent volumetric swelling. Fission gas release mechanisms are treated as for UO_2 fuel in the absence of additional information. The details

of these models were originally presented by Metzger et al. [36] and are reproduced here for completeness.

5.1.1.1 Thermal Model

The thermal model calculates the thermal conductivity and specific heat capacity of U_3Si_2. Two different models exist for both thermal conductivity and specific heat. The thermal conductivity options are denoted WHITE and SHIMIZU respectively, where the name corresponds to the main author of the paper where the model was proposed. The specific heat options that are available are WHITE and IAEA. The default models used in BISON are the WHITE models which are taken from White et al. [35]. The thermal conductivity correlation proposed by White et al. in W m^{-1} K^{-1} is:

$$k = 0.0151 \times T + 6.004 \tag{5.1}$$

where T is the temperature in K. For specific heat the correlation in J mol^{-1} K^{-1} is:

$$C_p = 0.02582 \times T + 140.5 \tag{5.2}$$

To obtain the specific heat SI units of J kg^{-1} K^{-1} one must divide the specific heat calculated by Eq. 5.2 by the molar mass for U_3Si_2 given as 0.77025773 kg mol^{-1}. Since White et al.'s data is new, legacy correlations were retained in BISON for thermal conductivity and specific heat. The SHIMIZU model for thermal conductivity was proposed by Shimizu [37]:

$$k = 7.98 + 0.0051 \times (T - 273.15) \tag{5.3}$$

where T is the temperature in K. The legacy correlation for specific heat (denoted IAEA) was presented in a Matos and Snelgrove IAEA technical report [38]:

$$C_p = 199 + 0.104 \times (T - 273.15) \tag{5.4}$$

The implementation of the thermal model allows any combination of thermal conductivity and specific heat models. For example the WHITE thermal conductivity model can be used with the IAEA specific heat correlation to perform investigative bounding studies.

5.1.1.2 Mechanical Model

Currently in the absence of additional data constant material properties are used for the Young's modulus and Poisson's ratio of U_3Si_2. The nominal values chosen are $E = 150$ GPa and $\nu = 0.177$. These Young's modulus and Poisson's ratio values were calculated from data presented by Shimizu [37] and Taylor and McMurtry [39] respectively.

5.1.1.3 Swelling and Densification

An empirical correlation was derived by Metzger et al. [36] from experimental data from Finlay et al. [40]. Metzger et al. converted the data in Figure 3 of Finlay et al. into swelling strain as a function of burnup (in FIMA) by utilizing a conversion factor from fission density (in fissions

per cubic centimeter) to FIMA of 3.63457×10^{-23}. The obtained empirical correlation is given by

$$\frac{V}{V_o} = 3.88008 \times Bu^2 + 0.79811 \times Bu \tag{5.5}$$

BISON requires the incremental volumetric swelling strain given by

$$\frac{\Delta V}{V_o} = (7.76016 \times Bu + 0.79811) \times \Delta Bu \tag{5.6}$$

where Bu is the burnup in FIMA. It is important to note that the above correlation is for the total volumetric swelling including both the gaseous and solid components. According to Metzger et al. U_3Si_2 is expected to undergo similar densification as UO_2 and therefore the ESCORE empirical model [41] was used:

$$\varepsilon_D = \Delta\rho_o(e^{\left(\frac{Bu\ ln(0.01)}{C_D Bu_D}\right)} - 1) \tag{5.7}$$

where ε_D is the densification strain, $\Delta\rho_0$ is the total densification that can occur (given as a fraction of theoretical density), Bu is the burnup, and Bu_D is the burnup at which densification is complete. For temperatures below 750 °C the parameter C_D is given by $7.2 - 0.0086(T - 25)$; above 750 °C it is 1.0 (T in °C). To eliminate the discontinuity in C_D, BISON uses $7.235 - 0.0086(T - 25)$ below 750 °C.

5.1.1.4 Fission Gas Release

Metzger et al. suggest that until future experiments are available that can provide accurate data on the fission gas release (FGR) in U_3Si_2 in pellet form that the FGR mechanisms be treated as similar to UO_2. The details of the fission gas release model in BISON are described in Pastore et al. [42]. The Simple Integrated Fission Gas Release and Swelling (SIFGRS) model has the ability to couple the fission gas generated to the gaseous swelling component. Because the swelling model for U_3Si_2 is the total swelling component, this coupling to gaseous swelling is not utilized. Therefore, any fission gas release only degrades the heat transfer between the fuel and the cladding. Due to the high thermal conductivity and subsequently low temperature of the fuel, it is expected that the fission gas released will be minimal during normal operation.

5.1.2 Sensitivity Analyses

Since many of the material properties for U_3Si_2 are based upon limited experimental data, sensitivity analyses can be used to determine which parameters have the greatest effect on output parameters of interest (e.g., fuel centerline temperature, cladding hoop stress). Prior to performing any sensitivity analyses a nominal example case was completed to illustrate the differences between UO_2 and U_3Si_2 behavior under normal operating LWR conditions. For this nominal example case traditional Zircaloy-4 was used for the cladding. A representative 2D axisymmetric example problem was used for the nominal case. The geometric dimensions and operational parameters were adapted from Williamson et al. [2] and Metzger et al. [36]. The problem simulates a 10-pellet fuel rodlet with Zr-4 cladding. Separate simulations were completed with UO_2 and

U_3Si_2 as the fuel respectively. The dimensions of the rodlet are typical of PWR fuel. The pellets had length and diameter of 11.9 mm and 8.2 mm, respectively. The cladding has a thickness of 0.56 mm for both materials for consistency, and a nominal initial radial gap of 80 μm was used. A second-order QUAD8 finite element mesh was used to approximate the geometry using 11 radial and 32 axial elements per pellet as illustrated in Figure 5.1. The cladding was modeled with 4 elements through the thickness and 326 elements axially.

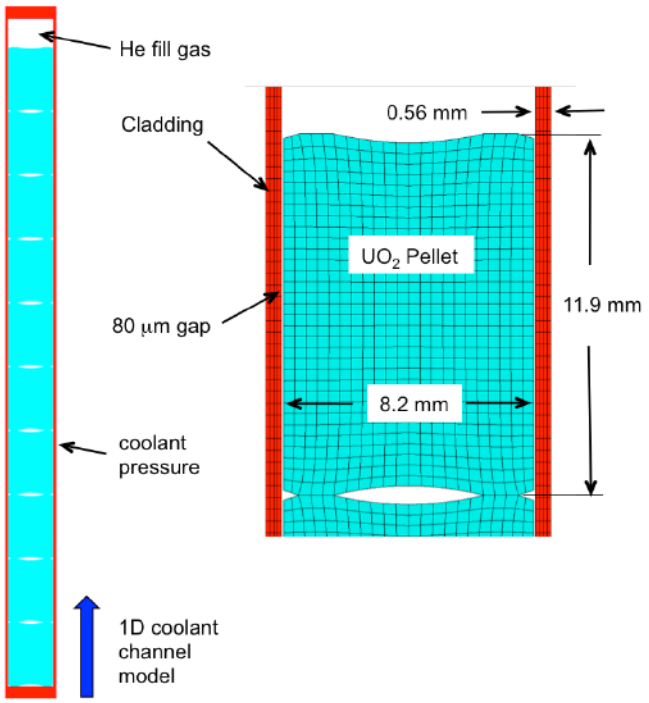

Figure 5.1: Geometry and mesh for the nominal example problem. Adapted from references [2, 36]

A simple power history is applied to the fuel. It is assumed the power rises linearly over approximately three hours and then is held constant at 25 kW/m for approximately 3.2 years. A symmetric axial profile is applied to the active fuel length of the rodlet such that the maximum power is applied at an axial position of 0.06162 m from the bottom of the fuel stack. A simple one-dimensional coolant channel model was used to calculate the convective heat transfer coefficient on the outside of the cladding. The operating conditions used are reproduced in Table 5.1.

A similar comparison to the one outlined above was presented in Metzger et al.'s paper; however in that case, fuel creep and relocation was turned off for the UO_2 fuel to be consistent with the elastic model used for U_3Si_2. Here we compare the results when using all of the information known about UO_2 to simulate the fuel.

Table 5.1: Operational parameters for the 2D axisymmetric example problem.

Parameter	Value	Units
Linear average power	250	$W\ cm^{-1}$
Fast neutron flux	7.5×10^{17}	$n\ m^{-2}\ s^{-1}$
Coolant Pressure	15.5	MPa
Coolant inlet temperature	580	K
Coolant inlet mass flux	3800	$kg\ m^{-2}\ s^{-1}$
Rod fill gas	Helium	-
Fill gas initial pressure	2.0	MPa
Initial fuel density	95% theoretical	-
Fuel densification	1% theoretical	-
Burnup at full densification	5	$MWd\ kgU^{-1}$

Figure 5.2(a) illustrates the fuel centerline, fuel surface, and cladding inner surface temperature histories. The higher thermal conductivity of U_3Si_2 results in a centerline temperature that is approximately 400 K lower than observed for UO_2. Consequently, the lower operating temperatures result in less thermal expansion, and the fuel-to-clad gap remains open longer. The point of contact occurs when the slope of the fuel surface and centerline curves change. UO_2 has a lower fuel surface temperature because relocation causes the fuel-clad gap to close more rapidly than in the U_3Si_2 case. Also, larger plenum volume and no fission gas release results in a lower plenum pressure with U_3Si_2 fuel as observed in Figure 5.2(b). While there is no fission gas release in the U_3Si_2 simulation, the plenum pressure constantly increases due to the closing of the fuel-to-clad gap due to thermal expansion. As the plenum volume continually decreases the internal pressure must increase, which is observed in Figure 5.2(b). The reason the uranium silicide simulations end at a lower burnup is due to the higher density of uranium in the U_3Si_2 matrix.

The mechanical properties and behavior of U_3Si_2 (e.g., creep) are not well known. Moreover, at the time of this analysis the optimal dimensions of U_3Si_2 fuel pellets for LWR applications are unclear. Therefore, a sensitivity study was completed using Sandia National Laboratories' Dakota [43] software with the input parameters chosen to be a scale factor on the fuel swelling, the Young's modulus, Poisson's ratio, coefficient of thermal expansion, and the initial pellet radius, where the output quantities of interest are fuel centerline temperature and the hoop stress on the exterior surface of the pellet. Figure 5.3 shows main effects plots for the two output parameters of interest. The independent parameters (e.g., scale factors and geometry) were given 3 distinct values in a histogram form resulting in 243 simulations in the multidimensional parameter study. The information in a main effects plot is such that a point represents the mean value of the output parameter for all simulations at which the corresponding input parameter had that particular value. The exterior hoop stress is compressive because the sensitivity study takes the last time step of the simulations once contact has already been established.

As expected the Young's modulus and Poisson's ratio have essentially zero effect on the center-

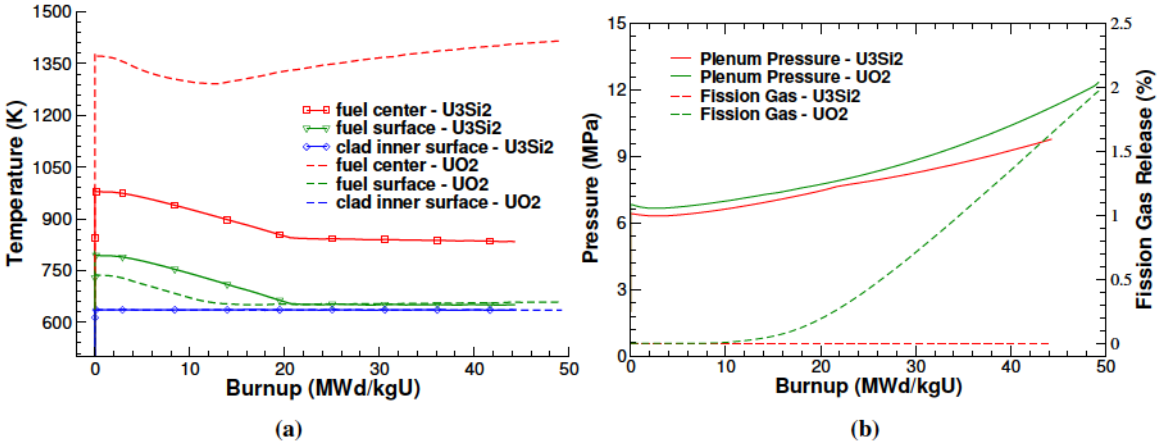

Figure 5.2: Comparisons between using U_3Si_2 and UO_2 in the example problem (a) fuel centerline, fuel surface, and clad inner surface temperatures, (b) plenum pressure and fission gas release.

line temperature and have a moderate affect on the exterior hoop stress. The input parameters with the most influence on centerline temperature and exterior hoop stress are the swelling factor and pellet radius. The radius of the fuel pellet is significantly correlated with the centerline temperature because the smaller the pellet radius the larger the fuel-to-clad gap. A large gap means reduced heat transfer and subsequently higher fuel temperatures. Contrarily, as the fuel radius is increased, the magnitude of the compressive stress on the exterior of the pellet decreases due to contact occurring prior to creep mechanisms having a strong compressive force on the expanding pellet. Keep in mind that the range of the mean centerline temperature is approximately 4 K. This is because the thermal conductivity of U_3Si_2 increases with temperature and the power history applied in the example case is constant. The parameter with greatest influence on centerline temperature would be the thermal conductivity, but since there is significant data already available [35, 37] it has been left out of the multidimensional parameter study presented here.

The results of the sensitivity studies were previously presented at TopFuel 2015 [44].

5.1.3 Bounding Studies

To provide some insight into areas where limited data is available and sensitivity analysis techniques cannot be employed, bounding studies have been completed to provide some understanding of the behavior of U_3Si_2. Two bounding investigations were completed using the U_3Si_2 models in BISON, one on fission gas release and one on solid and gaseous swelling.

The first study on fission gas release was concerned determining the effect of fission gas release on the centerline temperature in the example problem containing U_3Si_2 fuel and traditional Zircaloy-4 cladding. Because U_3Si_2 has a high thermal conductivity and the centerline temperature is low, it is expected that there will not be a large quantity of gas released. However, in the

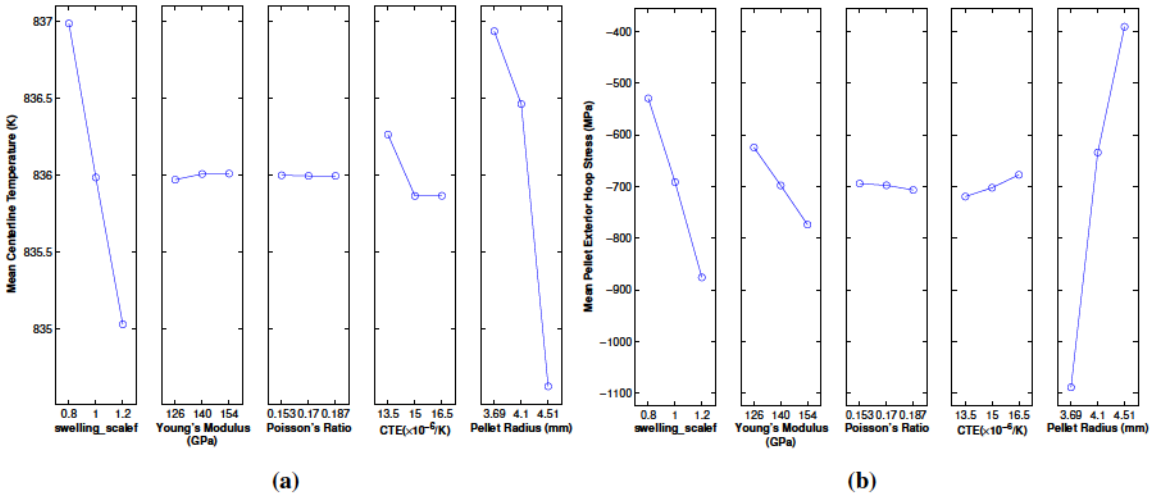

Figure 5.3: Main effects plots investigating the sensitivity of U3Si2 material properties on (a) the fuel centerline temperature and (b) the pellet exterior hoop stress at an axial location of 0.06162 m on the fuel rodlet. This location corresponds to the axial location of highest power.

absence of other data the fission gas mechanisms and diffusion coefficients used in the fission gas model are those of UO_2. From lower length scale investigations it has been proven that the diffusion coefficients of fission products in U_3Si_2 is different from UO_2. To investigate the effect of different diffusion coefficients, the grain boundary and intragranular diffusion coefficients for UO_2 were scaled by factors varying from 1 to 6.93e5 and plotting the fission gas released as a function of temperature as shown in Figure 5.4. The annotated number next to each data point corresponds to the scaling factor on the diffusion coefficients for that case. It is observed that even up to fission gas released percentages of 74.4 the centerline temperature only increased by approximately 400 K and is still well below any temperature of concern for U_3Si_2.

The second bounding study performed on U_3Si_2 was concerned with decoupling the fuel swelling model presented in Equation 5.5 into gaseous and solid swelling components. Three cases were investigated and compared: 1) no densification, and both gaseous and solid swelling, 2) no gaseous swelling, and both solid swelling and densification, 3) densification, and both gaseous and solid swelling. In order to be able to turn on and off gaseous swelling, the model in Equation 5.5 had to be decoupled into separate components. This was completed by utilizing the swelling only contribution from Figure 5 in Finlay et al.'s paper [40]. By plotting the solid only contribution and the BISON correlation on the same plot (see Figure 5.5) the onset of gaseous swelling can be approximated. After gaseous swelling begins the BISON curve includes both gaseous and solid swelling. By subtracting the solid contribution from the total swelling, the gaseous contribution can be determined.

Therefore, the volumetric strain increment for solid swelling is given by

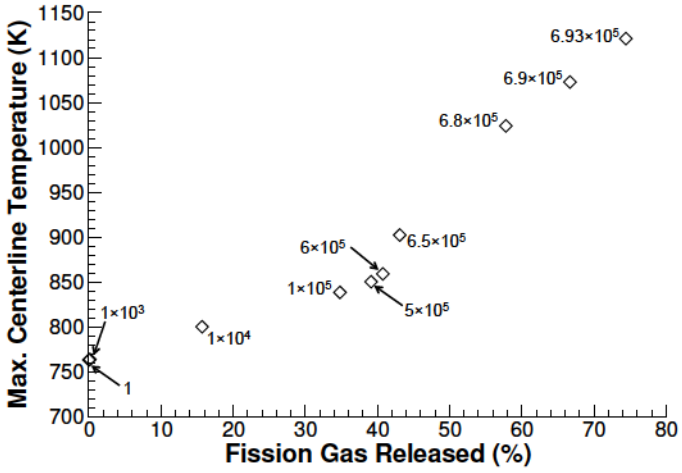

Figure 5.4: Centerline temperature as a function of fission gas released in U_3Si_2 by varying the intragranular and grain boundary diffusion coefficients.

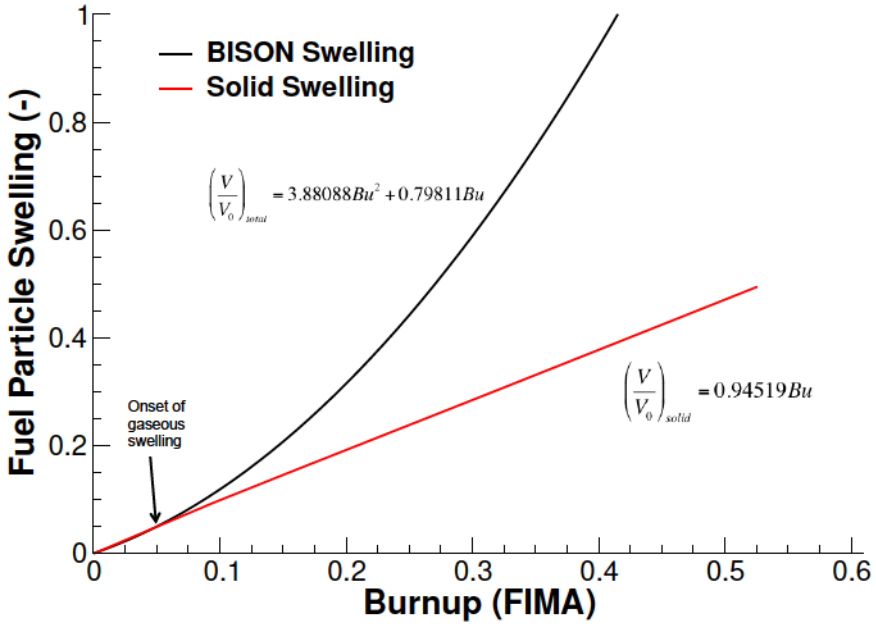

Figure 5.5: Illustration of BISON total swelling with the Finlay's [40] solid swelling component. The solid swelling component was used to decouple BISON's swelling into two separate components, solid and gaseous.

$$\left(\frac{\Delta V}{V_o}\right)_{solid} = 0.94519 \times \Delta Bu \tag{5.8}$$

where Bu is the burnup in FIMA. Below a burnup of 0.05 FIMA gaseous swelling is zero, otherwise the gaseous swelling is given by

$$\left(\frac{\Delta V}{V_o}\right)_{gaseous} = (7.76016 \times Bu + 0.79811) \times \Delta Bu - (0.94519 \times \Delta Bu) \tag{5.9}$$

In order to achieve some gaseous swelling the example problem used for the sensitivity studies had to be modified slightly to accumulate enough burnup. To achieve a higher burnup to reach and go beyond the onset of gaseous swelling the time of irradiation at power was doubled. Results were obtained for the hoop stress at the cladding interior and pellet exterior at an axial location of 0.06162 m corresponding to the highest power as a function of burnup for the three cases of interest as shown in Figure 5.6. In addition, results were obtained of the radial distribution of the hoop stress and total swelling within the fuel at the last time step as shown in Figure 5.7.

As expected the case with no fuel densification results in contact between the pellets and cladding being established earlier as shown in Figure 5.7(a) as the transition from compressive to tensile stress on the interior surface of the cladding occurs at an earlier burnup. The onset of gaseous swelling can see at a burnup of ~30 MWd/kgU. The case with no gaseous swelling results in a lower overall cladding stress as expected since the fuel is not pushing into the cladding as much. The hoop stress in the fuel is seen to be compressive due to resistance from the cladding. However, the magnitude of the compressive hoop stress at the fuel exterior is much higher than expected. This is likely attributed to no thermal and irradiation creep models being available for U_3Si_2. Future studies should focus on the development and investigation into creep behavior of U_3Si_2.

Based upon the hoop stress results at the exterior of the fuel presented in Figure 5.6(b) it was desired to investigate the hoop stress behavior radially through the pellet as shown in Figure 5.7(a). What the plot illustrates is that the significantly large hoop stress only occurs in the last finite element of the fuel pellet. The reason for this significant increase in swelling resulting in a larger hoop stress is the use of the radial power factor model that is BISON for UO_2. In absence of other data this was considered an acceptable approximation. Due to the radial power factor the burnup on the outer rim of the pellet is significantly higher than the burnup at the interior of the fuel and therefore the swelling and subsequently the hoop stress is higher in this region. A creep model for the fuel could help reduce the stress experienced at the pellet exterior.

5.2 Iron-Chromium-Aluminum (Fe-Cr-Al) Alloys

FeCrAl alloys are considered part of a class of materials known as advanced oxidation-resistant iron alloys and are one proposed cladding material for used in accident tolerant LWR fuel rods.

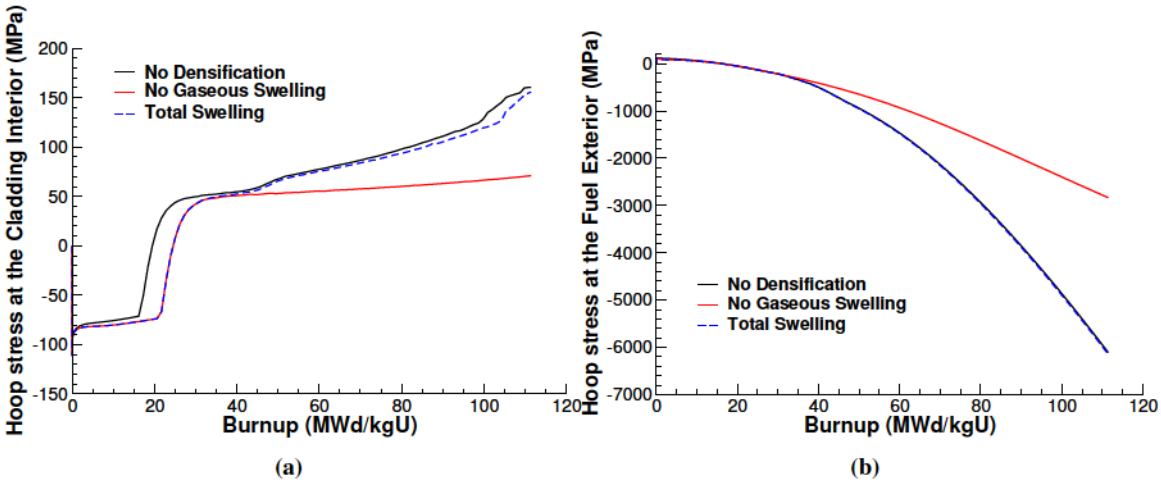

Figure 5.6: Bounding study results for U_3Si_2 swelling for (a) hoop stress on the interior of the cladding and (b) hoop stress on the exterior of the fuel pellet at an axial location of 0.06162 m on the rodlet. This axial location corresponds to the location of highest power.

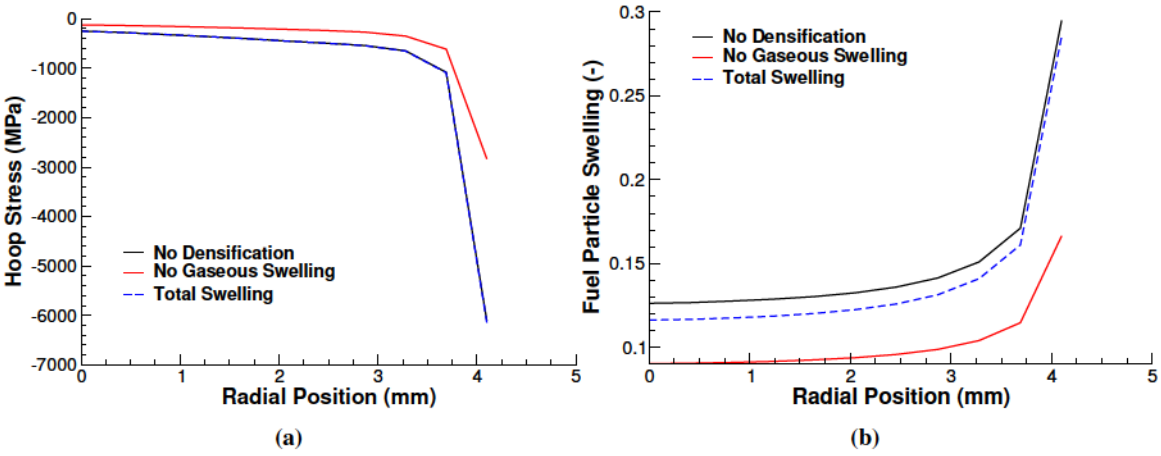

Figure 5.7: Bounding study results for U_3Si_2 swelling for at the last time step for (a) hoop stress as a function of radial position in the fuel and (b) total swelling as a function of radial position at an axial location of 0.06162 m on the rodlet. This axial location corresponds to the location of highest power.

Typically other dopants are included into the iron-chromium-aluminum structure to provide desired material behavior such as molybdenum, yttrium, titanium, and carbon. One of the advantages of FeCrAl alloys over their traditional zirconium based counterparts include an increased creep resistant at high temperatures, such as those experienced during design basis and beyond design basis accidents. Moreover, the oxidation rates of FeCrAl alloys are less than Zircaloy [45, 46]. Terrani et al. [45] performed oxidation tests in pure steam at atmospheric pressure, whereas Dryepondt et al. [46] performed oxidation tests at temperatures in the range of 800-1050°C. Additionally, the oxide layer that forms on the cladding prevents hydrogen ingress and hydride formation, which is prevalent in Zircaloy cladding. Thus, the risk of cladding failure due to the precipitation of circumferential hydrides during used fuel disposition is mitigated.

Some of the disadvantages and difficulties of using FeCrAl alloys as a cladding material include their lower melting points then Zircaloy. In addition research of various chromia (C_2O_3) forming steels found that the required chromium content for protective barrier formation in steam at 1200°C is in excess of 20% [47]. These chromium concentrations would limit the irradiation performance of the alloy [45]. Furthermore, there is limited data on the mechanical properties of FeCrAl alloys and their durability under mechanical stresses and irradiation [46]. For example, the creep data available for MA956 and PM2000 produced by Wasilkowska et al. [48] is limited to a few selected temperatures and is not presented in a manner that is easily implemented into BISON. This lack of data requires multiscale modeling to develop mechanistic material models and sensitivity studies to identify areas where further experiments are required.

5.2.1 Material Models

5.2.1.1 Thermal and Mechanical Models

To investigate the behaviour of FeCrAl cladding in a fuel performance setting and to identify areas where further research is required, a preliminary model of FeCrAl was added to BISON. The material model allows the selection of three different FeCrAl alloys: Kanthal APMT [49], PM2000 [50] and MA956 [51]. Using the information provided in the datasheets available from the manufacturers of these alloys, the thermophysical properties including specific heat capacity, thermal conductivity, modulus of elasticity, Poisson's ratio, and coefficient of thermal expansion (CTE) are calculated as a function of temperature from the tabulated data. For temperatures between the tabulated points linear interpolation is used. Note that the CTE data is provided as a mean value rather than instantaneous and therefore to obtain the correct thermal strain the method by Niffenegger and Reichlin [52] needs to be employed.

5.2.1.2 Swelling

It is expected that FeCrAl alloys will be subjected to irradiation induced swelling due to their cubic crystal structure. As an approximation for the swelling of FeCrAl alloys a simplistic model provided by Kurt Terrani from ORNL has been implemented in BISON. The estimated swelling rate is 0.05% per dpa. Using the same conversion factor as suggested above for irradiation creep (1×10^{25} n/m^2 = 0.9 dpa) the volumetric swelling strain rate is given by:

$$\dot{\varepsilon} = 4.5 \times 10^{-29} \phi \tag{5.10}$$

Integrating over time the volumetric swelling is given by

$$\varepsilon = 4.5 \times 10^{-29} \Phi \tag{5.11}$$

where Φ is the fast neutron fluence given in n/m^2.

5.2.1.3 Thermal and Irradiation Creep

When choosing a potential cladding material for accident tolerant applications, an understanding of the creep behaviour at normal operating and high temperatures as well as under irradiation conditions is of great importance. Two creep models exist for FeCrAl alloys, one for the commercial MA956 and one for a generic Fecralloy. The thermal creep correlation for MA56 is a Norton law based creep model proposed by Seiler et al. [53]:

$$\dot{\varepsilon} = \underbrace{A_0 \cdot \exp(\alpha T) \cdot \exp\left(-\frac{Q}{RT}\right)}_{\text{A}} \cdot \sigma^n \tag{5.12}$$

where Q is the activation energy, n is the creep exponent and α an additional factor. The creep behavior of MA956 is characterized by three regimes with independent sets of creep parameters. The transition from one regime to another takes place at the critical stress σ_{c1} and σ_{c2}. These critical stresses are calculated during the simulation by equating two equations with the different creep parameters in the two regimes. For example the first critical stress is defined as

$$\sigma_{c1} = \left(\frac{A_1}{A_2}\right)^{\frac{1}{n_2 - n_1}} \tag{5.13}$$

where $A_1(A_0, Q, \alpha, R, T)$ and n_1 are parameters in the range $\sigma < \sigma_{c1}$, and $A_2(A_0, Q, \alpha, R, T)$ and n_2 are parameters in the range $\sigma_{c1} < \sigma < \sigma_{c2}$, respectively. Table 5.2 lists the creep parameters of MA956 for the various stress regimes.

Table 5.2: Creep parameters of MA956

	A_0 $[MPa^{-n}s^{-1}]$	n [-]	Q [kJ/mol]	α $[K^{-1}]$
$\sigma < \sigma_{c!}$	78.978	4.9827	453	0.0
$\sigma_{c1} < \sigma < \sigma_{c2}$	3.466×10^{-124}	41.0	453	0.1
$\sigma > \sigma_{c2}$	8.68×10^{16}	5.2911	486	-0.0122

The model for thermal creep of Fecralloy was proposed by Saunders et al. [54]:

$$\dot{\varepsilon} = 5.96 \times 10^{-27} \sigma^{5.5} \exp\left(-\frac{47136}{T}\right) \tag{5.14}$$

where σ is the effective stress in Pa and T is the temperature in K. The model incorporated into BISON for irradiation creep of FeCrAl alloys suggested by Kurt Terrani from ORNL through

a personal communication. The coefficient for irradiation creep recommended by Terrani was 0.5×10^{-6} per MPa per dpa. Utilizing the following conversion factor: 1×10^{25} n/m^2 = 0.9 dpa a correlation for irradiation creep can be derived.

$$\dot{\varepsilon} = 4.5 \times 10^{-32} \sigma \phi \tag{5.15}$$

where σ is the effective stress in MPa and ϕ is the fast neutron flux in n/m^2-s.

5.2.2 Sensitivity Analyses

To demonstrate the behavior of FeCrAl alloys under light water reactor conditions similar baseline and sensitivity analyses as those for U_3Si_2 were completed. In these cases the fuel was kept as UO_2 and an MA956 cladding was used. Comparisons between the example problem utilizing traditional Zircaloy-4 cladding and MA956 are shown in Figure 5.8. Figure 5.8(a) presents the comparison of fuel centreline, fuel surface and cladding inner surface temperatures as a function of burnup. It is observed from the beginning of irradiation that the fuel rodlet with MA956 cladding has higher fuel centerline and surface temperatures then the Zircaloy clad rodlet. Significantly less creep is experienced by the MA956 resulting in the fuel-to-clad gap remaining open for a longer duration leading to higher fuel temperatures. The inner cladding surface temperature remains relatively constant for both simulations. The point of fuel-to-clad contact occurs at the points at which the slopes of the curves change (i.e. about 12 MWd/kgU and 38 MWd/kgU for the Zircaloy-4 and MA956 rods respectively).

Since the MA956 rodlet experiences higher fuel temperatures, the fission gas released from the fuel grain boundaries to the plenum region is higher than the Zircaloy-4 rodlet as illustrated in 5.8(b). Subsequently, the larger plenum and gap space within the fuel element due to less creep down of the cladding results in a lower pressure within the plenum. The magnitude of creep experienced by MA956 is very low at normal operating temperatures. However, it is unclear what the effect that irradiation creep would have on the behavior of MA956 at these temperatures. In Zircaloy-4 it is observed that thermal creep mechanisms are essentially negligible at normal operating temperatures (< 600 °C) where irradiation creep dominates, whereas at high temperatures (e.g. during a LOCA) thermal creep mechanisms are of greatest influence. Therefore, it is important to include irradiation effects of MA956 to see if the creep rate increases during normal operation as with Zircaloy-4.
While the example case above provides the nominal behaviour of MA956 cladding under normal operating conditions and highlights the limited creep experienced, there is still much not known about FeCrAl alloys. Moreover, the dimensions of an accident tolerant fuel rod are unclear. To gain a preliminary understanding of which mechanical and thermal properties, creep properties, and geometrical dimensions have the greatest influence on important rod properties such as the hoop stress and fuel centerline temperature, a sensitivity analysis was completed using Dakota [43].

Starting with the nominal example problem with MA956 cladding, the Young's modulus, Poisson's ratio, thermal conductivity, radial gap width, and cladding thickness were varied by $\pm$ 10%

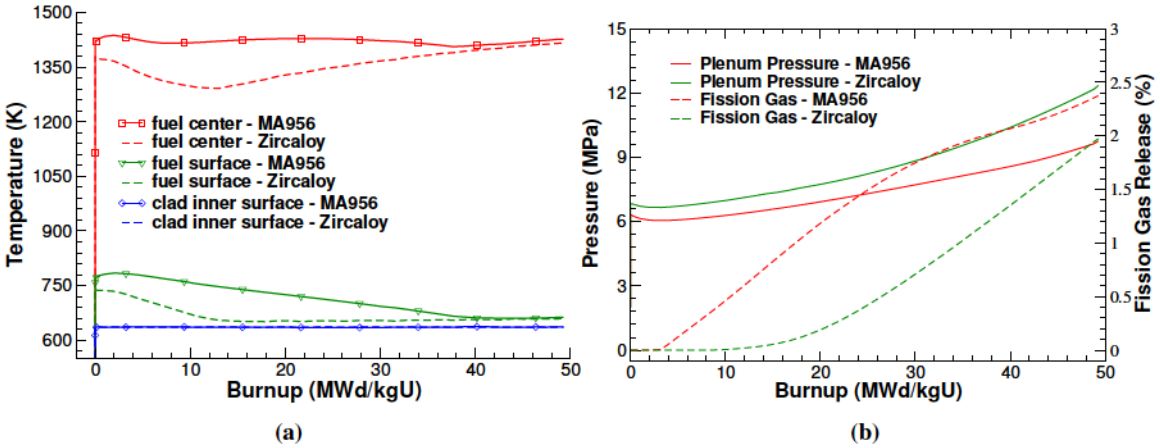

Figure 5.8: Comparisons between using U_3Si_2 and UO_2 in the example problem (a) fuel centerline, fuel surface, and clad inner surface temperatures, (b) plenum pressure and fission gas release.

to examine the effects of these parameters on hoop stress on the inner surface of the cladding and the fuel centerline temperature. Since the material properties vary as a function of temperature, a scale factor had to be used to properly vary these parameters. While varying the thermal creep parameters in Equation 5.12 would be of interest, initial investigations indicated that for the example problem investigated here the negligible creep strain experienced does not have an affect on the stress results. The main effects plots of the study are presented in Figure 5.9

As expected it is imperative that the dimensions of an accident tolerant fuel rod be determined as the clad thickness and initial gap between the fuel and cladding have a strong influence on the stress state of the clad and the fuel centerline temperature as seen by the large slopes in the main effects plots for these parameters. The final centerline temperature is strongly influenced by the initial gap size. A larger initial gap results in higher temperatures because gap closure takes longer to occur. Similarly, a larger thickness means more material for the heat to pass through causing a slight increase in the centerline temperature. These plots confirm the expected behavior when certain material parameters are varied. While the datasheets for the FeCrAl alloys provide values for the thermo-physical parameters at certain temperatures, it is uncertain if linearly interpolating between these values for temperature for which data is not provided is appropriate. Since the completion of this study the dimensions of the proposed FeCrAl claddings including inner and outer diameters and thickness have been decided. The sensitivity results here have been previously presented at TopFuel 2015 [44].

5.2.3 Bounding Studies

Preliminary bounding studies for FeCrAl alloys have been completed by Ryan Sweet at the University of Tennessee Knoxville. In these studies the upper and lower bounds were put on FeCrAl swelling, and thermal and irradiation creep. The lower bounds were zero, Fecralloy

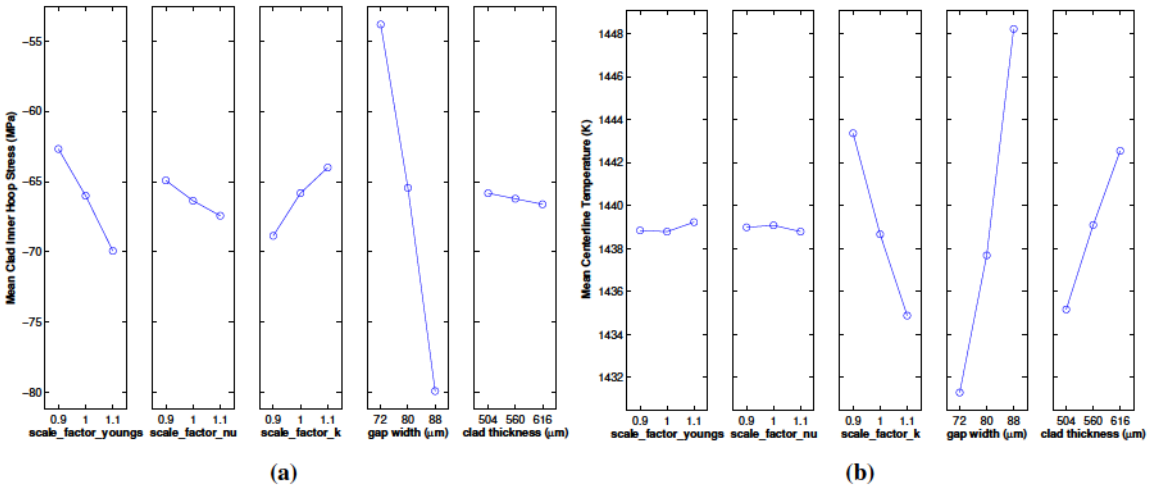

Figure 5.9: Main effects plots analyzing the sensitivity of MA956 material parameters including a scale factor on the Young's modulus and Poisson's ratio, thermal conductivity, gap width, and clad thickness on the (a) clad inner hoop stress and (b) centerline temperature in the example problem at an axial location of 0.06162 m. This location corresponds to the axial location of highest power.

creep, and zero for swelling, thermal creep, and irradiation creep respectively. The upper bounds were given by Equation 5.11, Zircaloy-4, and Equation 5.15, respectively. The power history used and the results of the bounding studies for FeCrAl are currently not available for publication from Ryan at this time.

5.3 Modeling of reflooding in full length cladding tube in a LOCA

A test case based on the geometry and test conditions used in one FLECHT experiment was prepared and tested using both coarse mesh (5x2)[1] and fine mesh (50x2) with different options to model reflooding of the full length cladding tube in a LOCA. The key input parameters are provided in Table 5.3. Figure 5.10 provides the simulated decay power used in the test. Figure 5.11 provides the axial power profile. Figure 5.12 provides the axial clad temperature profile at the start of reflooding.

Stainless steel 304 was used as the cladding tube materials in the test; however, due to the lack of material properties at high temperatures, constant thermal properties are assumed in the current test case: thermal conductivity = 21 W/m-K, specific heat = 500 J/kg-K, and density = 8030 kg/m^3.

Calculated clad temperature using the fine mesh (50x2) is shown in Figure 5.13. The response of the full length cladding tube in a reflooding test can be simulated using the BISON code.

[1]Number of elements in axial direction x number of elements in radial direction.

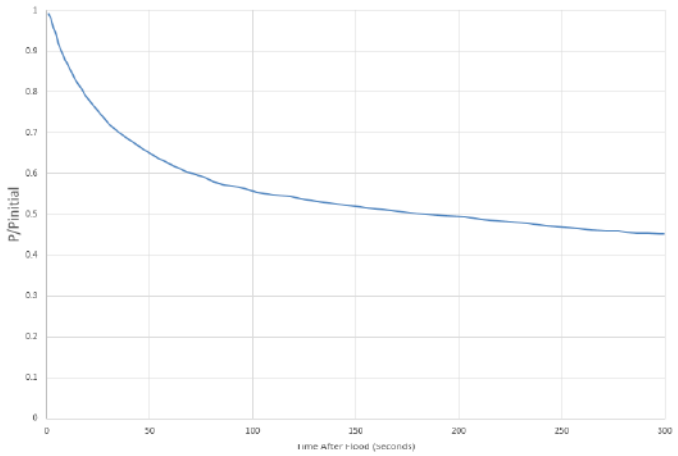

Figure 5.10: Power as a function of time.

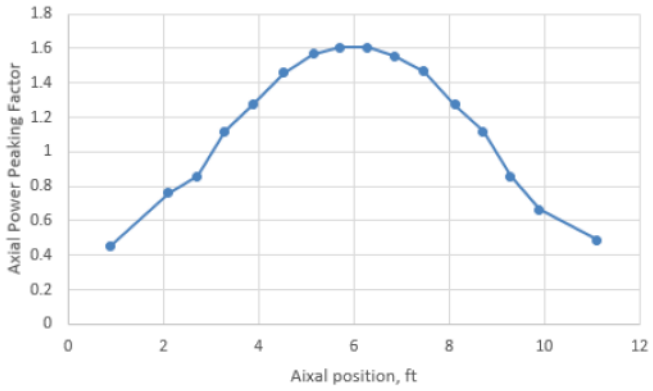

Figure 5.11: Axial power profile extracted from FRAPTRAN code [55].

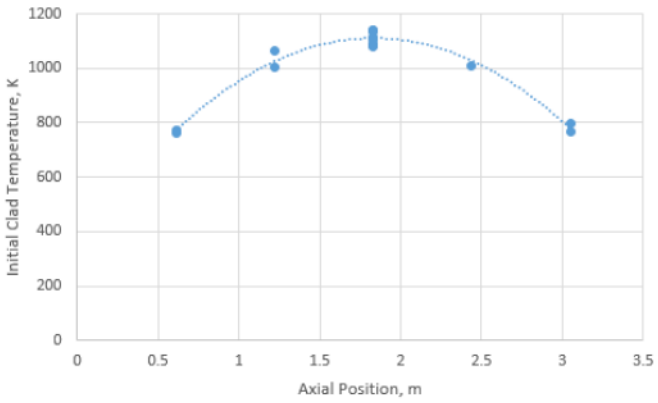

Figure 5.12: Initial clad axial temperature profile.

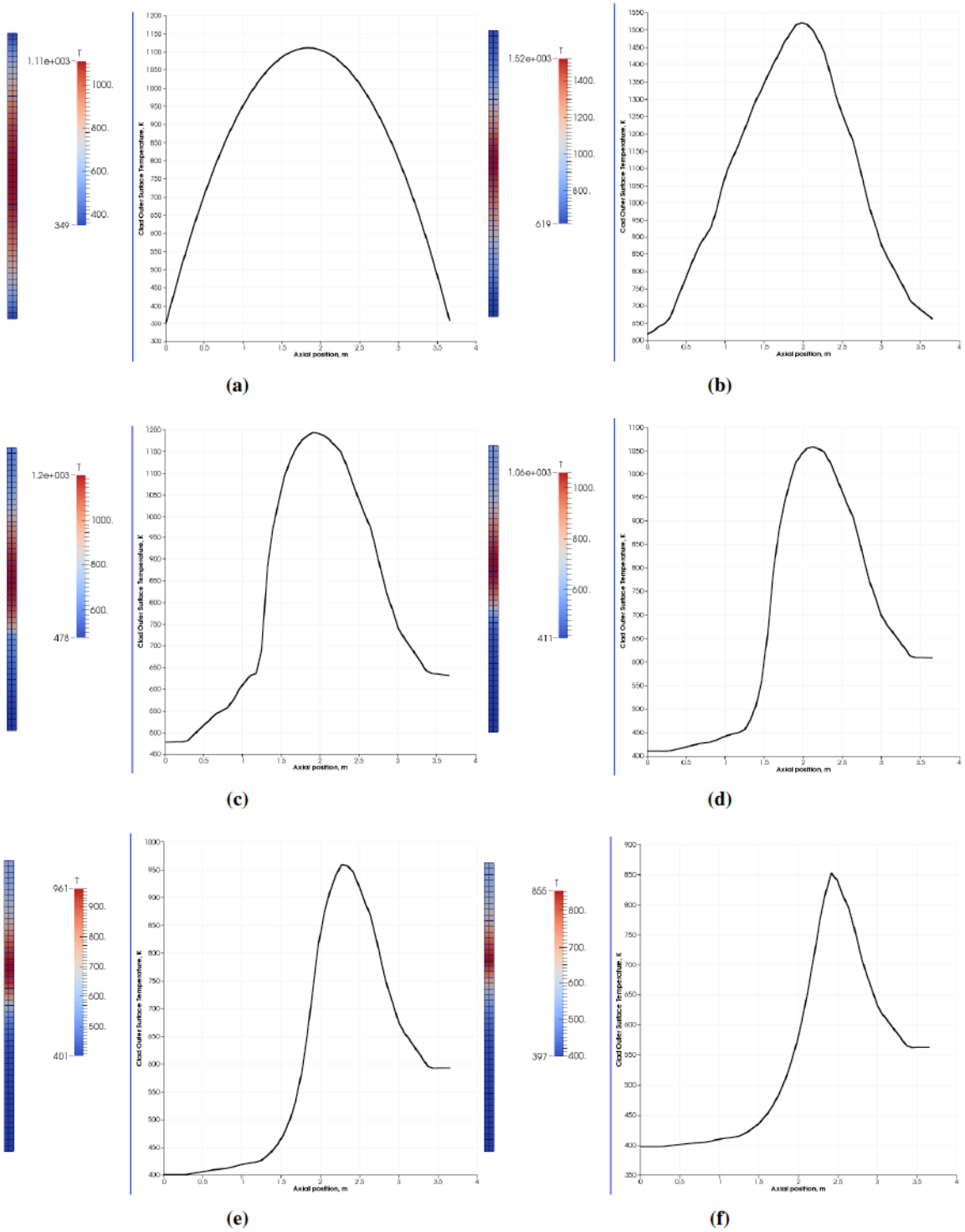

Figure 5.13: Full length cladding temperature calculated using BISON at different times during the reflood including (a) 0 sec, (b) 50 sec, (c) 100 sec, (d) 150 sec, (e) 200 sec, and (f) 250 sec.

Table 5.3: Input Parameters for Modeling Reflooding a in Full Length Cladding Tube in a LOCA

Parameters	Value	Unit
Clad OD	0.010719	m
Clad ID	0.0095	m
Clad thickness	0.00061	m
Clad outer radius	0.005359	m
Clad inner radius	0.00475	m
Length of Cladding Tube	3.6576	m
Flooding rate	0.0508	m/s
Peak Power	4.07	kW/m
Inlet Pressure	172370	Pa
Inlet Temperature	312	K

Figure 5.14 gives the clad outer surface temperature at the upper part of the cladding tube without quenching (a) and with the quenching model (b). The small temperature peak before quench appears to be not physical. The reason could be the mesh for modeling the axial direction may not be fine enough when the quenching model is turned on, creating a high axial temperature gradient. This needs to be investigated. The theory behind the reflooding capability and how to use the capability in a BISON simulation are documented in the BISON theory and user manuals respectively.

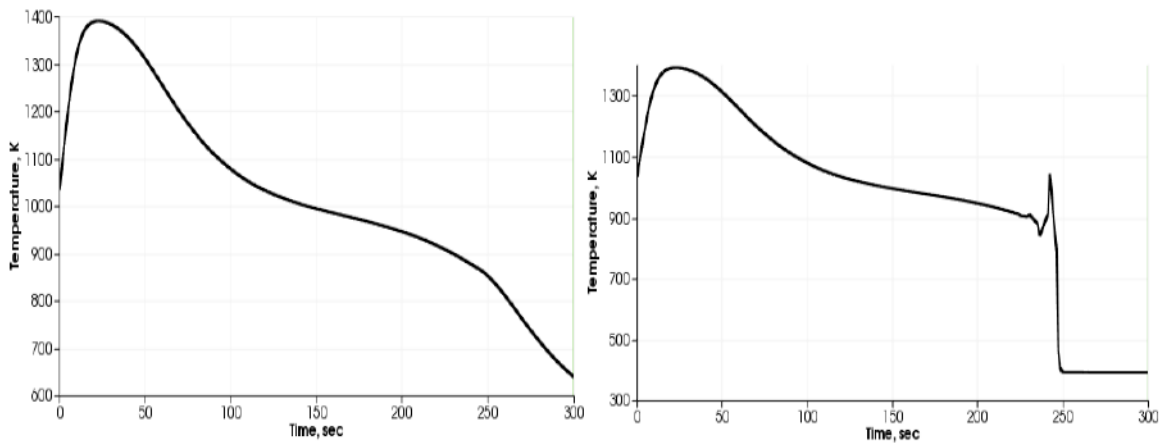

Figure 5.14: Clad outer surface temperature at an axial elevation of 2.4 m calculated using BISON for (a) a reflood without quenching and (b) a reflood with quenching.

6 Summary

This report presented the density functional theory, molecular dynamics, mesoscale and engineering scale developments in regards to the accident tolerant fuel concepts of U_3Si_2 fuel and FeCrAl alloy claddings. The work was completed as part of the DOE's NEAMS ATF HIP. Additional areas requiring attention have been identified in each of the sections. Work will continue at all length scales eventually leading to coupled multiphysics between the different length scales. A greater focus on accident scenarios, such as loss of coolant accidents and reactivity insertion accidents, will occur in the next fiscal year.

7 Acknowledgements

Funding for this work is from the DOE Nuclear Energy Advanced Modeling and Simulation program.

Bibliography

[1] S. Bragg-Sitton, B. Merrill, M. Teague, L. Ott, K. Robb, M. Farmer, M. Billone, R. Montgomery, C. Stanek, M. Todosow, and N. Brown. Advanced fuels campaign: enhanced LWR accident tolerant fuel performance metrics. Technical Report INL/EXT-13-29957, Idaho National Laboratory, 2013.

[2] R. L. Williamson, J. D. Hales, S. R. Novascone, M. R. Tonks, D. R. Gaston, C. J. Permann, D. Andrs, and R. C. Martineau. Multidimensional multiphysics simulation of nuclear fuel behavior. *Journal of Nuclear Materials*, 423:149–163, 2012.

[3] J. D. Hales, R. L. Williamson, S. R. Novascone, D. M. Perez, B. W. Spencer, and G. Pastore. Multidimensional multiphysics simulation of TRISO particle fuel. *Journal of Nuclear Materials*, 443:531–543, 2013.

[4] J. D. Hales, S. R. Novascone, B. W. Spencer, R. L. Williamson, G. Pastore, and D. M. Perez. Verification of the BISON fuel performance code. *Annals of Nuclear Energy*, 71:81–90, 2014.

[5] M. R. Tonks, D. Gaston, P. C. Millett, D. Andrs, and P. Talbot. An object-oriented finite element framework for multiphysics phase field simulations. *Computational Materials Science*, 51:20–29, 2012.

[6] G. Kresse and J. Hafner. *Ab initio* molecular dynamics for open-shell transition metals. *Physical Review B*, 48:13115–13118, 1993.

[7] G. Kresse and J. Furthmüller. Efficiency of ab-initio total energy calculations for metals and semiconductors using a plane-wave basis set. *Journal of Computational Materials Science*, 6:15–50, 1996.

[8] G. Kresse and J. Furthmüller. Efficient iterative schemes for *ab initio* total-energy using a plane-wave basis set. *Physical Review B*, 54:11169–11186, 1996.

[9] J. P. Perdew, K. Burke, and M. Ernzerhof. Generalized Gradient Approximation Made Simple. *Physical Review Letters*, 77(18):3865–3868, 1996.

[10] S. L. Dudarev, D. N. Manh, and A. P. Sutton. Effect of mott-hubbard correlations on the electronic structure and structural stability of uranium dioxide. *Philosophical Magazine Part B*, 75:613–628, 1997.

[11] H. Okamoto. Si-U (Silicon-Uranium. *Journal of Phase Equilibria and Diffusion*, 34:167–168, 2013.

[12] M. I. Baskes. Modified embedded-atom potentials for cubic materials and impurities. *Physical Review B*, 46(5):2727–2742, 1992.

[13] A. Breche, C. Rado, O. Rapaud, C. Guéneau, and J. Rogez. Thermodynamic study of the U-Si system. *Journal of Nuclear Materials*, 84:10–107, 2009.

[14] T. Kumagai, S. Izumi, S. Hara, and S. Sakai. Development of bond-order potentials that can reproduce the elastic constants and melting point of silicon for classical molecular dynamics simulation. *Journal of Computational Materials Science*, 39:457–464, 2007.

[15] A. Patra and D. L. McDowell. Crystal plasticity-based constitutive modeling of irradiated bcc structures. *Philosophical Magazine*, 92(7):861–887, 2012.

[16] A. Patra and D. L. McDowell. Continuum modeling of localized deformation in irradiated bcc materials. *Journal of Nuclear Materials*, 432(1–3):414–427, 2013.

[17] R. A. Lebenshon and C. N. Tomé. A self-consistent anisotropic approach for the simulation of plastic deformation and texture development of polycrystals: application to zirconium alloys. *Acta metallurgica et materialia*, 41(9):2611–2624, 1993.

[18] K. G. Field, M. N. Gusset, Y. Yamamoto, and L. L. Snead. Deformation behavior of laser welds in high temperature oxidation resistant Fe-Cr-Al alloys for fuel cladding applications. *Journal of Nuclear Materials*, 454(1–3):352–358, 2014.

[19] K. G. Field, X. Hu, K. C. Littrell, Y. Yamamoto, and L. L. Snead. Radiation tolerance of neutron-irradiated model Fe-Cr-Al alloys. *Journal of Nuclear Materials*, 465:746–755, 2015.

[20] K. G. Field, X. Hu, K. Littrell, Y. Yamamoto, R. H. Howard, and L. L. Snead. Stability of model Fe-Cr-Al alloys under the presence of neutron radiation. Technical report, Oak Ridge National Laboratory (ORNL): High Flux Isotope Reactor (HFIR), 2014.

[21] B. Ye, J. Rest, Y.S. Kim, G. Hofman, and B. Dionne. Dart analysis of irradiation behavior of U-Mo/Al dispersion fuels. *Journal of Nuclear Technology*, 191:27–40, 2015.

[22] J. Rest and G.L. Hofman. Kinetics of recrystallization and fission-gas-induced swelling in high burnup UO2 and U3Si2 nuclear fuels. *Fundamental Aspects of Inert Gases in Solids*, 279:443–456, 1991.

[23] M.A. Feraday, G.H. Chalder, and K.D. Cotnam. Irradiation behavior of cored U3Ai fuel elements. *Journal of Nuclear Applications*, 4:148–153, 1968.

[24] J. Rest. Grass-sst: a comprehensive mechanistic model for the prediction of fission-gas behavior in UO2-base fuels during steady-state and transient conditions. Technical Report NUREG/CR-0202, Argonne National Laboratory, 1978.

[25] J. Rest and G.L. Hofman. Dynamics of irradiation-induced grain subdivision and swelling in U3Si2 and UO2 fuels. *Journal of Nuclear Materials*, 210:187–202, 1994.

[26] G.L. Hofman and J. Rest. Comparison of irradiation behavior of different uranium silicide dispersion fuel element designs. In *Proceedings of the 17th International Meeting on Reduced Enrichment for Research and Test Reactors (RERTR)*, Williamsburg, USA, 1994.

[27] J. Rest. The dart dispersion analysis research tool: A mechanistic model for predicting fission-product-induced swelling of aluminum dispersion fuels. Technical Report ANL-95/36, Argonne National Laboratory, 1995.

[28] Y.S. Kim and G.L. Hofman. Fission product induced swelling of U-Mo alloy fuel. *Journal of Nuclear Materials*, 419:291–301, 2011.

[29] I.I. Konovalov. Basic properties of fuel determining its behavior under irradiation. In *International Meeting on Reduced Enrichment for Research and Test Reactors*, Las Vegas, NV, USA, 2000.

[30] C.L. Whitmarsh. The significance of irradiation-induced creep on reactor performance of a zircaloy-2 pressure tube. Technical Report ORNL-281, Oak Ridge National Laboratory, 1962.

[31] B. Watkins and D.S. Wood. The significance of irradiation-induced creep on reactor performance of a zircaloy-2 pressure tube. *ASTM Selected Technical Papers*, 458:226–280, 1969.

[32] P.C. Barnett. Calculation of fast neutron flux in reactor pressure tubes and experimental facilities. Technical Report AECL-3167, Atomic Energy of Canada Limited, 1968.

[33] C.G.S. Pallai, A. K. Dua, and P. Raj. Thermal conductivity of U_3O_8 from 300 K to 1100 K. *Journal of Nuclear Materials*, 288:87–91, 2001.

[34] P.G. Lucuta, Hj. Matzke, and R.A. Verrall. Thermal conductivity of hyperstoichiometric SIMFUEL. *Journal of Nuclear Materials*, 223:51–60, 1995.

[35] J.T. White, A.T. Nelson, J.T. Dunwoody, D.D. Byler, D.J. Safarik, and K.J. McClellan. Thermophysical properties of U_3Si_2 to 1773 k. *Journal of Nuclear Materials*, 464:275–280, 2015.

[36] K. E. Metzger, T. W. Knight, and R. L. Williamson. Model of U_3Si_2 fuel system using BISON fuel code. In *Proceedings of the International Congress on Advances in Nuclear Power Plants, 2014*, Charlotte, NC, USA, 2014.

[37] H. Shimizu. The properties and irradiation behavior of U_3Si_2. Technical Report NAA-SR-10621, Atomics International, 1965.

[38] J. E. Matos and J. L. Snelgrove. Research reactor core conversion guidebook-Vol 4: Fuels (Appendices I-K). Technical Report IAEA-TECDOC-643, International Atomic Energy Agency, 1992.

[39] K. M. Taylor and C. H. McMurtry. Synthesis and Fabrication of Refractory Uranium Compounds. Technical Report ORO-400, Carborundum Co., 1960.

[40] M.R. Finlay, G.L. Hofman, and J.L. Snelgrove. Irradiation behaviour of uranium silicide compounds. *Journal of Nuclear Materials*, 325:118–128, 2004.

[41] Y. Rashid, R. Dunham, and R. Montgomery. Fuel analysis and licensing code: FALCON MOD01. Technical Report EPRI 1011308, Electric Power Research Institute, 2004.

[42] G. Pastore, L. Luzzi, V. Di Marcello, and P. Van Uffelen. Physics-based modeling of fission gas swelling and release in UO_2 applied to integral fuel rod analysis. *Nuclear Engineering and Design*, 256:75–86, 2013.

[43] B.M. Adams, L.E. Bauman, W.J. Bohnhoff, K.R. Dalbey, M.S. Ebeida, J.P. Eddy, M.S. Eldred, P.D. Hough, K.T. Hu, J.D. Jakeman, L.P. Swiler, and D.M. Vigil. Dakota, a multilevel parallel object-oriented framework for design optimization, parameter estimation, uncertainty quantification, and sensitivity analysis: Version 5.4 user's manual. Technical Report SAND2010-2183, Sandia National Laboratories, 2009, Updated April 2013.

[44] J. D. Hales and K. A. Gamble. Preliminary Evaluation of FeCrAl Cladding and U-Si Fuel for Accident Tolerant Fuel Concepts. In *TopFuel 2015*, Zurich, Switzerland, 2015.

[45] K. A. Terrani, S. J. Zinkle, and L. L. Snead. Advanced oxidation-resistant iron-based alloys for LWR fuel cladding. *Journal of Nuclear Materials*, 448:420–435, 2014.

[46] S. Dryepondt, B. A. Pint, and E. Lara-Curzio. Creep behavior of commercial fecral foils: Beneficial and detrimental effects of oxidation. *Materials Science and Engineering A*, 550:10–18, 2012.

[47] B. A. Pint, K. A. Terrani, M. P. Brady, T. Cheng, and J. R. Keiser. High temperature oxidation of fuel cladding candidate materials in steam-hydrogen environments. *Journal of Nuclear Materials*, 440:420–427, 2013.

[48] A. Wasilkowska, M. Bartsch, U. Messerschmidt, R. Herzog, and A. Czyrska-Filemonowicz. Creep mechanisms of ferritic oxide dispersion strengthened alloys. *Journal of Materials Processing Technology*, 133:218–224, 2003.

[49] Kanthal APMT (Tube) Datasheet. http://kanthal.com/en/products/material-datasheets/tube/kanthal-apmt/, 2012.

[50] Schwarzkopf Plansee PM2000 Datasheet. http://www.matweb.com/search/datasheet.aspx?matguid=21e9ec9a0

[51] Special Metals INCOLOY Alloy MA956 Datasheet. http://www.specialmetals.com/documents/Incoloy%20alloy%20MA956.pdf.

[52] M. Niffenegger and K. Reichlin. The proper use of thermal expansion coefficients in finite element calculations. *Journal of Nuclear Engineering and Design*, 243:356–359, 2012.

[53] P. Seiler, M. Bäker, and J. Rösler. Variation of creep properties and interfacial roughness in thermal barrier coating systems. *Advanced Ceramic Coatings and Materials for Extreme Environments*, 32:129–136, 2011.

[54] S. R. J. Saunders, H. E. Evans, M. Li, D. D. Gohil, and S. Osgerby. Oxidation growth stresses in an alumina-forming ferritic steel measured by creep deflection. *Oxidation of Metals*, 48:189–200, 1997.

[55] M.E. Cunningham, C.E. Beyer, F.E. Panisko, and P.G. Medvedev. FRAPTRAN: A Computer Code for the Transient Analysis of Oxide Fuel Rods. Technical Report NUREG/CR-6739, Volume 1, Pacific Northwest National Laboratory, 2001.